Fe-ZSM-5 outperforms Al-ZSM-5 in paraffin cracking by increasing the olefinicity of C3-C4 products

Kurbanova, Anastasia; Zákutná, Dominika; Gołąbek, Kinga; Hraníček, Jakub; Dugulan, Achim Iulian; Diddams, Paul; Hsieh, Ming-Feng; Bats, Nicolas; Přech, Jan

DOI
10.1016/j.cej.2024.156032

Publication date
2024

Document Version
Final published version

Published in
Chemical Engineering Journal

Chemical Engineering Journal 499 (2024) 156032

Contents lists available at ScienceDirect

Chemical Engineering Journal

journal homepage: www.elsevier.com/locate/cej

Fe-ZSM-5 outperforms Al-ZSM-5 in paraffin cracking by increasing the olefinicity of C_3-C_4 products

Anastasia Kurbanova [a], Dominika Zákutná [b], Kinga Gołąbek [a], Jakub Hraníček [c], Achim Iulian Dugulan [d], Paul Diddams [a], Ming-Feng Hsieh [e], Nicolas Bats [e], Jan Přech [a,*]

[a] Department of Physical and Macromolecular Chemistry, Faculty of Science, Charles University, Hlavova 2030/8, 128 43 Prague 2, Czech Republic
[b] Department of Inorganic Chemistry, Faculty of Science, Charles University, Hlavova 2030/8, 128 43 Prague 2, Czech Republic
[c] Department of Analytical Chemistry, Faculty of Science, Charles University, Hlavova 2030/8, 128 43 Prague 2, Czech Republic
[d] Radiation Science & Technology (FAME), Delft University of Technology, Mekelweg 15, 2629 JB Delft, the Netherlands
[e] Johnson Matthey Technology Centre, Belasis Avenue, Billingham TS23 1LB, United Kingdom

ARTICLE INFO

Keywords:
Heterogeneous catalysis
Zeolites
Fe-ZSM-5
Paraffin
Cracking
Propene

ABSTRACT

Iron-modified Al-ZSM-5 increases selectivity to propene, a key petrochemical resulting from fluid catalytic cracking (FCC). However, the type and role of active iron species remain unclear, hindering efforts to streamline the design of selective FCC additives. Here, we investigated Al-free Fe-ZSM-5 catalysts containing iron species in the form of framework Fe^{3+}, extra-framework Fe^{3+}, oxidic clusters, and oxide micro aggregates in n-octane cracking (FCC model) to assess their effect on catalytic cracking. DR-UV–Vis spectroscopy, ^{57}Fe Mössbauer Spectroscopy, FTIR studies of pyridine adsorption, and n-octane cracking tests at 500 °C revealed that framework-associated coordinatively unsaturated Fe^{3+} species, which induce strong Lewis acidity, are responsible for paraffin cracking initiation, whereas bulk iron oxides on the zeolite surface are inactive. In comparison with Al-ZSM-5, Fe-ZSM-5 increases the olefinicity of the valuable C_3-C_4 fractions (selectivity to propene and butenes) and promotes aromatization reactions due to the lower relative strength of Fe-induced Brønsted acid sites and dehydrogenation properties. As shown by our ^{57}Fe Mössbauer study (performed at −269 °C) of the catalyst in calcined, spent, and regenerated states, Fe-ZSM-5 deactivation is associated with the loss of tetrahedrally coordinated Fe^{3+} species. Therefore, tuning Fe-ZSM-5 C_3-C_4 selective FCC additives requires stabilizing framework Brønsted and framework-associated Lewis acid sites while decreasing the concentration of iron oxide species. Ultimately, these findings may enable us to meet the demand for propene derived from FCC cracking, which is expected to grow in the foreseeable future.

1. Introduction

In oil refineries, fluid catalytic cracking (FCC) converts low-value, high-molecular-weight crude oil hydrocarbons into lighter, higher-value fractions, such as gasoline, diesel, and jet fuel [1,2]. The first FCC plant came on stream more than 80 years ago, yet the demand for FCC use and upgrading has been rising ever since. In response, FCC plant productivity has been upgraded using various strategies, including reactor modification (e.g., adding a two-stage regeneration unit to decrease catalyst deactivation rate [3]), catalyst re-design (e.g., applying additives, such as ZSM-5, to increase selectivity to light olefins – propene and butenes [4]), and feed optimization (e.g., adding hydrotreating units to remove sulfur, nitrogen and metals, thereby increasing conversion and decreasing coke yield [5]). The expected fall in the need for transportation fuel in context with the global demand for a transition to renewable energy and consequent adaptation to oil-to-chemical processes re-defines the key modern-day challenges for FCC [6]. These challenges include co-processing waste or renewable feedstocks [7,8] and integrating catalytic additives to drive selectivity to higher-value petrochemicals, such as benzene-toluene-xylenes fraction (BTX) [9] and light olefins, especially propene [10].

Propene is a key building block for the polymer industry to produce polypropylene and acrylonitrile [11,12]. Moreover, propene is one of the primary olefin feedstocks for alkylation processes, such as benzene alkylation to cumene (phenol synthesis intermediate) [13,14]. The global propene market is predicted to steadily grow at a 3–4%

* Corresponding author.
E-mail address: jan.prech@natur.cuni.cz (J. Přech).

https://doi.org/10.1016/j.cej.2024.156032
Received 29 June 2024; Received in revised form 5 September 2024; Accepted 19 September 2024
Available online 27 September 2024

compound annual growth rate (CAGR) in the foreseeable future (2024–2032) as its derivatives have a wide range of applications in the packaging, automotive, and construction industries [15]. Most propene (60–65%) is produced by steam cracking alongside ethene. The second largest production (30%) derives from FCC, while the remainder comes from propane dehydrogenation and metathesis processes [12]. The increasing demand for propene vs. ethene creates a gap in the market, which gives rise to additional propene production from processes other than steam cracking. In this context, FCC stands out as a candidate for enhancing propene yields because FCC is less energy-demanding than steam cracking, and its product distribution can be modified through catalyst optimization [11].

A typical commercial FCC catalyst is a hierarchical material consisting of an active zeolite phase dispersed in an aluminosilicate matrix composed of activated alumina, metal traps (for Ni and V metals), filler (kaolin clay), and a binder (typically derived from colloidal silica or alumina; when derived from the latter, the binder contributes to Lewis acidity) [16]. The combination of components is tuned to provide (a) balanced acidity (both Brønsted and Lewis), (b) hierarchical pore sizes (mesopores and micropores) for easy diffusion of reactants and products to active sites within catalyst particles, (c) hydrothermal and mechanical attrition stability, (d) optimal particle density for fluidization, (e) metal impurity tolerance, and (f) low coke selectivity. The main zeolite used in FCC catalysts is a faujasite-type Y large-pore zeolite, most often in its partially dealuminated (ultra-stabilized) form, containing rare-earth metals (Rare Earth Ultrastable Y zeolite, REUSY) [17]. Lanthanum in cationic positions, located mainly in sodalite cages, increases structural stability, but controlled steaming provides ultra-stabilization by improving hydrothermal stability and introducing additional mesoporosity. In addition to the main catalyst, secondary co-catalysts, also known as “additives”, are often used as well, including MFI-type aluminosilicate zeolites (ZSM-5).

As a co-catalyst, ZSM-5 improves the production of light olefins (propene and butenes) and gasoline octane number in FCC by selectively cracking low octane components, including linear alkanes (paraffins), and by promoting isomerization reactions, thus increasing branching in C_{6+} (gasoline range) isomers [18]. In fact, this medium-pore zeolite with strong acid sites (Al-ZSM-5) has been doing so since the 1980s, but refiners continuously aim at finetuning co-catalyst activity to the desired product selectivity [19]. Case in point, recent data published by both academic [20–23] and industrial [24,25] researchers has shown that introducing iron species into Al-ZSM-5 enhances selectivity to light olefins and aromatics, which are more valuable than C_2-C_4 paraffins.

Fe^{3+}/Al-ZSM-5 outperforms Al-ZSM-5 in FCC regardless of the synthesis procedure followed to introduce Fe into this aluminosilicate zeolite. For instance, self-pillared Fe-Al-ZSM–5 resulting from partial isomorphous substitution of Fe^{3+}, introduced by direct synthesis, displays higher selectivity to light olefins, particularly propene (27%) and ethene (16 %), than nanosheet Al-ZSM-5 zeolite (24 and 15% selectivity, respectively) in n-heptane cracking at 600 °C. [20] In n-octane cracking, also at 600 °C, Fe^{3+} ion exchange increases BTX yield from 2% over parent H^+/Al-ZSM-5 to 11% over ion-exchanged Fe^{3+}/Al-ZSM-5 by strengthening the adsorption of light olefins on Fe^{3+} Lewis acid sites, thus increasing their surface coverage, as shown by DFT calculations of adsorption enthalpy change [21]. Moreover, when prepared by wet impregnation, Fe^{3+}/Al-ZSM-5 (2 wt% Fe) is not only more selective to light olefins (60%) and propene (23%) but also more stable than its parent Al-ZSM-5 [23]. Combined, these findings confirm that incorporating iron species in ZSM-5 facilitates the production of olefins and aromatics.

Notwithstanding these consistent findings, the mechanism whereby active Fe^{3+} species enhance ZSM-5 performance [20,21,23–25] in FCC remains unclear since the complexity of Fe and Al containing systems together with differences in experimental approaches reported in the literature hinder efforts to streamline the design of selective FCC additives [19]. To this end, we must understand in depth the role and properties of these active Fe species. Nevertheless, Fe-ZSM-5 is already known to contain tetrahedrally coordinated framework Fe^{3+} species, tetrahedrally and octahedrally coordinated extra-framework species (Fe^{3+} ions and oligomeric Fe_xO_y oxidic clusters in channels or on the surface), and oxidic Fe_xO_y micro aggregates on the zeolite surface [26]. Fe^{3+} in a tetrahedrally coordinated framework site generates Brønsted acid sites [27]. Lewis acidity [14] can be induced through trivalent coordinatively unsaturated Fe^{3+} species either bound to the framework or located in extra-framework positions (resulting from calcination [28]). Correlating these catalytically active Fe^{3+} species of Fe-ZSM-5 with the final product distribution in FCC may, therefore, enable us to design selective co-catalysts because this process proceeds via different mechanistic pathways depending on the catalyst properties [2].

Considering the above, the present study aims at gaining fundamental understanding of the effect of various iron species in ZSM-5 zeolite catalysts on their catalytic performance in hydrocarbon cracking. Various catalytically active Fe^{3+} species were identified on Al-free Fe-ZSM-5 zeolites in n-octane cracking at 500 °C through a detailed characterization of these catalysts and correlation of the characterization data with the final product distributions. For this purpose, we hydrothermally synthesized a series of iron silicates with a ZSM-5 structure (containing framework and extra-framework iron species) and a Fe^{3+} impregnated reference (containing oxidic aggregates) differing in their iron species and overall iron content. The oxidation state and coordination of the iron species were analyzed by ^{57}Fe Mössbauer and DR-UV–vis spectroscopy, whereas the type and concentration of iron-induced acid sites were assessed by FTIR spectroscopy of an adsorbed pyridine molecular probe. Iron content and speciation were correlated with the product distribution of n-octane cracking over Fe-ZSM-5 catalysts vs. Al-ZSM-5 reference. Based on the characterization of these iron species in a spent (coked) and regenerated Fe-ZSM-5 after cracking, we determined their stability under reaction conditions. Gaining such fundamental understanding of the Fe species that are responsible for cracking activity and increased selectivity to light olefins and aromatics is essential to develop methods for introducing and stabilize them in FCC catalysts and for putting new olefin selective FCC additives into real use.

2. Experimental

2.1. Catalyst synthesis

Al-free Fe-ZSM-5 samples were synthesized following previously reported protocols [29,30]. The samples are denoted as Fe-ZSM-5 (R), where R is the Si-to-Fe molar ratio determined by elemental analysis. In a representative synthesis of Fe-ZSM-5 (21) 13.1 g of tetraethyl orthosilicate (TEOS, 98%, Sigma Aldrich) were mixed with 3.1 g of ethanol (Technical grade – 96.5%, Penta Chemicals) at room temperature (solution 1). In parallel, solution 2 was prepared by adding 1.3 g of Fe $(NO_3)_3$*$9H_2O$ (98%, Sigma Aldrich) to 30 g of distilled water. Both solutions were stirred separately for 1 h. Subsequently, solution 2 was added drop-by-drop to solution 1, forming the silica-iron oxide gel, which was left to homogenize for 2 h under stirring. Then, 11.8 g of tetrapropylammonium hydroxide (TPAOH, Sigma Aldrich, 40% solution in water) and 6.7 g of distilled water were added to the gel under stirring. With a molar composition of 100 TEOS: 100 ethanol: 5 $Fe(NO_3)_3$: 40 TPAOH: 3800 H_2O, the final mixture was further stirred for 1.5 h and then transferred to a 100 mL Teflon-lined autoclave. Hydrothermal synthesis was performed under agitation (60 rpm) at 175 °C for 120 h. After the hydrothermal synthesis, the autoclave was cooled, and the solid product was filtered, washed with distilled water until reaching filtrate pH 7-8, and left to dry overnight at 60 °C.

Fe-ZSM-5 samples (17) and (28) were prepared by scaling up (10 fold) the synthesis to a 1000 mL Parr® stainless steel autoclave equipped with turbine stirring, heating, and cooling systems. For these samples, the stirring rate was set to 300 rpm. All other operations, including gel preparation, were the same.

The dry zeolites were calcined to remove the organics and to convert the zeolites into their proton forms using the following procedure: 1) samples were heated at 5 ℃/min under an inert atmosphere (N_2) up to 450 ℃ and held for 1.5 h; 2) the gas was switched to air, and the samples were heated up to 550 ℃ at 1℃/min, remaining at this temperature for 10 h. Such inert heat-up conditions minimize the loss of framework iron species.

Fe_2O_3/S-1 was prepared by wet (in solvent excess) iron impregnation on commercially available silicalite-1 (S-1 (R), where R is the Si/Al molar ratio determined by ICP-MS. In detail, 0.36 g of $Fe(NO_3)_3{\cdot}9\ H_2O$ (Sigma Aldrich, 98%), equivalent to 5 wt% of Fe, were dissolved in 50 mL of deionized water. Then, 1 g of silicalite-1 (Si/Al = 380) catalyst was added to the solution. The mixture was heated to 90 ℃ under stirring overnight until evaporating all the water. The sample was further dried at 60 °C overnight and calcined at 550℃ (2 °C/min heating ramp) for 6 h.

Al-ZSM-5 (R) zeolites, where R is the Si-to-Al molar ratio determined by ICP-MS (25 and 60, respectively), were purchased from Zeolyst Int. in NH_4^+ form. The samples were calcined under airflow at 550 ℃ for 6 h at 2 °C/min to convert them into proton form before the catalytic tests.

2.2. Characterization

X-ray powder diffraction (XRD) analysis was conducted using a Bruker D8 Advance diffractometer, equipped with a Linxeye XE-T detector in Bragg–Brentano geometry, employing Cu Kα (λ = 0.15406 nm) radiation.

Nitrogen adsorption/desorption isotherms were measured on a Micromeritics 3Flex volumetric Surface Area Analyzer at −196 °C. Before sorption measurements, all samples underwent outgassing under a turbomolecular pump vacuum on a Micromeritics Smart Vac Prep instrument. Outgassing involved heating from ambient temperature up to 110 °C at 1 °C/min until reaching a residual pressure of 13.3 Pa. After heating at 110 °C for 1 h, the temperature was increased to 250 °C (1 °C/min) and maintained for 8 h. The BET area (S_{BET}) was calculated using the BET method [31,32] based on adsorption data in the range of a relative pressure p/p_0 = 0.05–0.20. Micropore volume (V_{mic}) was assessed using the t-plot method [33].The total adsorption capacity (V_{tot}) at a relative pressure $p/p_0 = 0.95$ was determined using the BJH algorithm from the desorption branches of the isotherms. The spent catalyst sample was outgassed only by heating from ambient temperature up to 80 °C with a heating rate of 1 °C/min until the residual pressure of 13.3 Pa was reached. After heating at 80 °C for 1 h, the temperature was increased to 110 °C (1 °C/min) and maintained for 6 h.

Diffuse reflectance ultraviolet–visible spectroscopy (DR-UV–Vis) analysis was performed on a Cary 4000 UV–Vis Spectrophotometer equipped with a $BaSO_4$ integration sphere, against $BaSO_4$ as a 100% reflectance reference. These measurements were performed in a wavelength range of 200–800 nm and processed using the Kubelka-Munk function.

^{57}Fe Mössbauer spectroscopy was performed at room temperature on a Wissel spectrometer (with a ^{57}Co γ-source) using transmission geometry and a proportional detector without an applied magnetic field. The spectrometer was calibrated with a standard (α-Fe foil) and the spectra fitting procedure of the Wissel NORMOS program. The percentage of spectral contribution (W, %) of each iron species in zeolite samples was determined using Eq. 1, where $A_{Fe\ t}^{3+}$, $A_{Fe\ oct}^{3+}$, and $A_{Fe\ ox}^{3+}$ are the depths of the signal of the for Fe^{3+}tetrahedral, Fe^{3+}octahedral and Fe^{3+} oxide, subspectra, respectively.

$$W_{spectral\ \ contribution} = \frac{A_{Fe^{3+}}}{A_{Fe_t^{3+}} + A_{Fe_{oct}^{3+}} + A_{Fe_{ox}^{3+}}} \quad (1)$$

^{57}Fe Mössbauer spectra at −269 °C were collected on a conventional constant-acceleration spectrometer using a ^{57}Co (Rh) source. Velocity calibration was performed using an α-Fe foil at room temperature. The Mössbauer spectra were fitted and spectral contributions were calculated using the Mosswinn 4.0 program [34].

Acid sites were quantified based on Fourier transform infrared (FT-IR) spectroscopy studies using pyridine as probe molecule (py-FTIR). The samples were pressed into self-supporting wafers with a density of 10 mg/cm^2, placed in a custom-made *in-situ* glass IR cell (with KBr windows), and activated under vacuum (10^{-4} Pa) at 450 °C for 4 h, saturated with an excess of pyridine (≥99.9%; Sigma-Aldrich®) vapors (465 Pa) at 150 °C for 20 mins, and then evacuated at the same temperature to remove gaseous and physisorbed pyridine molecules. The number/fraction of strong acid sites was quantified by FTIR-monitored desorption at 250, 350 and 450 °C. The concentrations of Brønsted and Lewis acid sites were calculated from the integral intensities of the 1545 cm^{-1} band assigned to pyridinium ions (PyH^+) and of the 1455 cm^{-1} band assigned to pyridine coordinatively bonded to Lewis acid sites (PyL) using molar absorption coefficients of 1.09 and 1.71 cm^2 μmol^{-1} for the PyH^+ and PyL bands, respectively [35]. The concentration of acid sites in the spent catalyst in coked state (after three cracking cycles) [36] was quantified by evacuation (10^{-4} Pa) at room temperature and exposure to an excess of Pyridine vapors (465 Pa) for 10 min, also at room temperature, followed by evacuation. This adsorption step was repeated three times to ensure that all accessible acid sites were occupied by pyridine instead of water. The desorption step was performed under vacuum (10^{-4} Pa) at 150 °C for 20 min (as described above). All spectra were recorded on a Nicolet 6700 FT-IR Spectrometer equipped with an MCT detector at a spectral resolution of 4 cm^{-1}.

SEM images were acquired under a JEOL JSM-IT800 microscope using a secondary electron detector. All samples were deposited on conductive carbon tape mounted onto the SEM holder.

Elemental analysis was performed by inductively coupled plasma mass spectrometry (ICP-MS) on an Agilent 7900 ICP-MS spectrometer (Agilent Technologies, Inc., USA.). To determine the Fe, Si, Al, and Na content, 50 mg of catalyst were dissolved in 1.8 mL of HNO_3 (67–69%, ANALPURE®), 5.4 mL of HCl (34–37%, ANALPURE®) and 1.8 mL of HF (47–51 %, ANALPURE®) and placed into a closed Teflon vessel. The vessel was then transferred to a microwave (Speedwave® XPERT, Berghof) and heated at 210 °C (5 °C/min) for 25 min. Once cooled, the solutions were supplemented with 12 mL of H_3BO_3 to form a complex with the excess of HF and further microwaved at 190 °C (5 °C/min) for 10 min. The resulting solutions were diluted with distilled water for analysis.

Thermogravimetric analysis (TGA) of spent catalysts (in the coked state after cracking tests) was performed on a Setaram SETSYS Evolution 1750 thermal analyzer by heating approximately 10 mg of each sample in 100-μl corundum (Al_2O_3) crucibles from 25 to 750 °C in an oxidizing atmosphere with a 5 °C/min ramping rate.

2.3. n-Octane cracking catalytic experiment

n-Octane cracking catalytic experiments were conducted in a glass fixed-bed up-flow reactor with an inner diameter of 10 mm equipped with a K-type thermocouple, measuring the catalyst bed temperature. The catalyst was pressed, crushed, and sieved into a fraction with a particle size of 0.2–0.5 mm and then mixed with inert SiC (0.5 mm particle size). For Fe-ZSM-5 and Fe_2O_3/S-1, a mixture of 600 mg catalyst and 200 mg SiC was charged into the reactor. Catalyst activation was performed at 500 °C under a synthetic air (20 vol% O_2 in N_2) flow of 60 ml/min overnight, with an initial heating step at 100 °C for 2 h for water removal. n-octane cracking was performed at 500 °C and ambient pressure. The weight hourly space velocity (WHSV) was 2 h^{-1}. For the Al-ZSM-5 reference samples, the mass of the catalyst and SiC were adapted to match the Fe-ZSM-5 (17, 21) conversion and catalyst bed length (1.5 cm). For Al-ZSM-5 (25), 10 mg of catalyst (WHSV=122 h^{-1}) were diluted with 1.9 g of SiC; for Al-ZSM- 5 (60), 175 mg of catalyst (WHSV=7h^{-1}) were diluted with 1.6 g of SiC. Nitrogen was used as carrier gas. n-Octane partial pressure was 10 kPa. The catalytic reactor

was online connected to an Agilent 7890 gas chromatograph equipped with a non-polar Agilent J&W HP-PONA column 50 m x 0.2 mm × 0.5 μm and serially connected to TCD (for hydrogen) and FID (for hydrocarbons) detectors. Product identification was based on a comparison with pre-injected standards of hydrocarbons and hydrogen.

Equations **Eq. 2** – **Eq. 12** were used to calculate the conversion (X) of n-octane (*n-C8*) in wt.%, yield (Y) of hydrocarbon products (C_n, where n is the number of carbon fraction, C, e.g. C_1 is methane) in wt. %, selectivity to liquid petroleum gas or LPG ($C_{3's}$ + $C_{4's}$ paraffins and olefins) S_{LPG} (%), C_3 and C_4 olefinicity (%), average molecular weight (MW) of the reactor effluent (Ef) in g/mole and H_2 as wt% on feed, BTX yield (Y_{BTX}, wt.%) and dry gas yield ($Y_{dry\ gas}$, wt.%)

$$X = 100 - (n\text{-}C_{8\ unreacted})\ (wt.\%) \quad (2)$$

$$Y = \frac{C_n\ product\ GC - FID\ area}{Sum\ of\ all\ products\ GC\ areas} * 100(wt.\%) \quad (3)$$

$$S_{LPG} = \frac{Y_{LPG}}{X} * 100\ (\%) \quad (4)$$

$$Y_{C_3\ total} = Y_{propane} + Y_{propene}(wt.\%) \quad (5)$$

$$C_{3\ olefinicity} = \frac{Y_{propene}}{Y_{C_3\ total}} * 100\%\ (\%) \quad (6)$$

$$Y(C_{4=}) = Y_{butene-1} + Y_{isobutene} + Y_{trans-but-2-ene} + Y_{cis-but-2-ene}\ (wt.\%) \quad (7)$$

$$Y_{C_4} = Y_{butane} + Y_{isobutane}\ (wt.\%) \quad (9)$$

$$Y_{C_4 total} = Y_{C_4} + Y_{C_{4=}}\ (wt.\%) \quad (10)$$

$$C_{4\ olefinicity} = \frac{Y_{C_{4=}}}{Y_{C_4\ total}} * 100\%\ (\%) \quad (11)$$

$$H_{2\ volumetric\ fraction\ (TCD)} = \frac{H_{2\ TCD\ signal\ observed}}{100\%\ H_2\ TCD\ signal} * 100\%(\%) \quad (11)$$

$$Ef(MW) = \frac{((Y_{C_1}) * MW(C_1) + \cdots + Y_{C_n} * MW(C_n))}{(Y(C_1) + \cdots + Y(C_n))}\ (g/mole) \quad (12)$$

$$Y(H_{2\ as\ wt.\%\ feed}) = \frac{H_{2\ TCD} * 2}{Ef\ (MW)}(wt.\%\ on\ feed) \quad (13)$$

$$Y_{BTX} = Y_{benzene} + Y_{toluene} + Y_{xylenes}(wt.\%) \quad (14)$$

$$Y_{dry\ gas} = Y(H_2) + Y(CH_4) + Y(C_2H_6) + Y(C_2H_4)\ (wt.\%) \quad (15)$$

2.4. Propane dehydrogenation catalytic experiment

Propane dehydrogenation experiments were performed according to the catalytic setup used for n-octane cracking (see 2.3.), at 500 °C as well, based on ref. [37]. The catalyst preparation and activation procedures were also the same as those used for n-octane. During the catalytic experiment, the total feed flow rate was 80 mlN/min and the feed contained 5 mol % of propane (purity grade 3.5, Linde) diluted with N_2. The catalyst and SiC amounts were also selected to match the catalyst bed length (1.5 cm) of the n-octane tests: for Fe-ZSM-5 (28) and Fe_2O_3/S-1 600 mg of catalyst were diluted with 200 mg SiC (corresponding to WHSV=0.8 h^{-1}), while for Al-ZSM-5 (25) 100 mg were mixed with 1.7 g SiC (WHSV=4.7 h^{-1}). In a blank experiment, 1.9 g of SiC were loaded into the reactor. Products were quantified using an online connected GC Agilent 7890 equipped with HP-PLOT/Al_2O_3 capillary column (50 m × 0.32 mm × 8 μm) and serially connected TCD and FID detectors.

3. Results and discussion

3.1. Characterization of Fe-zeolite catalysts

This study aims to identify the role of different Fe species in Al-free ZSM-5 zeolites in the paraffin cracking reaction. For this purpose, several Fe-ZSM-5 catalysts with different Si/Fe ratios were prepared by hydrothermal synthesis to introduce iron as a framework atom. In addition, Fe_2O_3/S-1 was prepared by wet impregnation (of $Fe(NO_3)_3$ aqueous solution), resulting mainly in Fe_2O_3 oxide species and in a small share of extra-framework Fe^{3+} species. Two Al-ZSM-5 catalysts with different Si/Al molar ratios (25 and 60 respectively) served as reference materials.

All XRD patterns (**Figure S1, S2, Supporting information (SI)**) of hydrothermally synthesized Fe-ZSM-5 zeolites displayed the characteristic diffraction lines of the MFI topology. No additional phase was detected by this technique. Notably, all Fe-ZSM-5 samples, except Fe-ZSM-5 (17), remained white after calcination, indicating the absence of non-framework Fe oxide species [30]. Fe-ZSM-5 (17) was slightly rusty, indicating the presence of some oxidic species, but the color was not accompanied by additional diffraction lines of iron oxides, so none of the Fe oxide domains were large enough to provide XRD reflections (**Figure S2, SI**). The peaks corresponding to α-Fe_2O_3 species [38] at 2θ values of 33.2° and 35.5° (marked with *, **Figure S2, SI**) were only detected in Fe_2O_3/S-1, in line with the rusty color of the sample.

The textural properties of the Fe-ZSM-5, Fe_2O_3/S-1, and Al-ZSM-5 reference materials were analyzed by N_2 physisorption at −196 °C (Table 1). Fe_2O_3/S-1 had a BET area of 326 m^2/g and a total pore volume of 0.15 cm^3/g. The isotherm is classified as type I (**Figure S3, SI**) but contains a low-pressure step (uptake in the range of p/po = 0.2–0.3), which is typical of high-silica MFI (Silicalite-1) when using nitrogen as adsorbate [39]. All Fe-ZSM-5 materials showed similar textural properties, with 407–455 m^2/g BET area and 0.11–0.13 cm^3/g micropore volume (V_{mic}) (Table 1). The shapes of the N_2 adsorption isotherms of Fe-ZSM-5 (88, 66, 41) are classified as type I, typical of microporous materials [40,41] (**Figure S3, SI**). Conversely, the isotherms of samples with a low Si/Fe molar ratio (17, 21) display a gradual increase and a hysteresis loop at higher p/p_o, which likely originates from intercrystalline adsorption when smaller crystals form agglomerates, thus providing additional voids [18].

SEM imaging (**Figure S4, SI**) confirmed that Fe-ZSM-5 (17, 21) consisted of aggregates (0.3–0.5 μm diameter) of smaller spherical crystals. Conversely, Fe-ZSM-5 (41, 66, 88) samples had uniform cube-like crystals with 0.2–0.3 μm diameter. SEM images of Fe_2O_3/S-1 showed bulk iron oxide particles of various sizes located on the external surface of silicalite-1 crystals with 4 μm diameter (see **Figure S4, SI**).

The incorporation and coordination of Fe species were analyzed by diffuse reflectance ultraviolet–visible spectroscopy, with all samples in a calcined, ambient dehydration state. Fe-ZSM-5 samples showed similar spectra with intense absorption bands between 200 and 300 nm (Fig. 1**. A** and **B**). Absorption bands below 250 nm have been previously attributed to isolated tetrahedral Fe^{3+} ions. In turn, bands between 250–300 nm correspond to isolated Fe^{3+} ions in higher (octahedral) coordination state [42,43]. Additionally, absorption intensity gradually increases from around 300 nm, with the amount of Fe in samples increasing from Si/Fe = 88 to Si/Fe = 17 (indicated by a black arrow in Fig. 1**.A** and **B)**. Absorption bands between 300 and 450 nm correspond to Fe^{3+} ions in small oligo-nuclear oxidic clusters (and dimers), while bands above 450 nm are indicative of oxidic micro aggregates of Fe_xO_y [44,45]. In the spectrum of the hydrothermally synthesized Fe-ZSM-5 (17), the absorption in this area (300–600 nm) suggests the presence of all aforementioned Fe species. This result is consistent with the color of the calcined sample (rusty). Fe_2O_3/S-1 spectrum show absorption in all the above regions, peaking around 300–600 nm, attributed to extra-framework Fe^{3+} oxides and oligo-nuclear clusters. These findings are in line with the impregnation procedure.

Table 1
Textural properties (N_2 physisorption analysis), Si/Fe, Si/Al molar ratios and Fe wt. % (ICP-MS), and acidity of Fe-ZSM-5, Fe_2O_3/S-1, Al-ZSM-5 – concentration of Brønsted and Lewis acid sites calculated from IR studies of pyridine sorption.

Sample code	S_{BET} m^2/g	V_{mic} (cm^3/g)	V_{tot} (cm^3/g)	150 °C		450 °C	
				Brønsted acid sites (μmol/g)	Lewis acid sites(μmol/g)	Brønsted acid sites(μmol/g)	Lewis acid sites(μmol/g)
Fe-ZSM-5 (17)	400	0.12	0.26	269	159	–	65
Fe-ZSM-5 (21)	414	0.12	0.30	242	99	–	59
Fe-ZSM-5 (28)	455	0.13	0.26	260	120	–	50
Fe-ZSM-5 (41)	411	0.12	0.22	181	80	19	36
Fe-ZSM-5 (66)	407	0.12	0.21	140	79	26	29
Fe-ZSM-5 (88)	411	0.11	0.21	136	79	12	27
Al-ZSM-5 (25)	431	0.16	0.20	565	76	161	29
Al-ZSM-5 (60)	404	0.16	0.22	171	48	132	21
Silicalite-1 (380)	317	0.12	0.18	–	–	–	–
Fe_2O_3-S-1(Fe – 4.3 wt %)	325	0.13	0.15	–	–	–	–

^{57}Fe Mössbauer Spectroscopy analysis (Fig. 1**.C-G,** Table 2) was performed at room temperature to acquire more detailed information about iron speciation in Fe-ZSM-5 materials. The spectra of all Fe-ZSM-5 samples were refined, showing only Fe^{3+} ions in low and high coordination states; no Fe^{2+} was detected using this technique. The isomer shift (IS, δ) values below 0.3 mm/s indicate that Fe^{3+} species occupy tetrahedral coordination, while IS>0.3 mm/s^{-1} is characteristic of octahedral coordination [26,46,47]. Mössbauer spectra of samples with low Fe content in the sample (≤1.6 wt%, Fe-ZSM-5 (88, 66 and 41), see Table 2) were refined, showing broad singlet signals, corresponding to Fe^{3+} in the paramagnetic state, with an isomer shift of 0.24——0.27 mm·s^{-1}. This value of isomer shifts corresponded to tetrahedrally coordinated framework Fe^{3+} [26,29,47]. The absence of the octahedrally coordinated iron species signals observed in the DR-UV–vis may be caused by the low overall Fe concentration of these species, which is likely below the limit of detection of the technique (0.04 wt% ^{57}Fe), arising from the low natural abundance of ^{57}Fe isotope (2 %). Based on our Mössbauer spectroscopy data, we do not rule out the presence of octahedrally coordinated Fe^{3+} species, but their content should be low.

Mössbauer spectra of samples with a high amount of Fe (Fe-ZSM-5 (17, 21)) were sharper and indicated 2 different Fe species. For Fe-ZSM-5 (21), the spectrum was deconvoluted into a singlet with an isomer shift (δ) of 0.23 mm·s^{-1} corresponding to Fe^{3+} in tetrahedral coordination (with spectral contribution W=73(2)%, where 2 stands for standard deviation), and a doublet with an isomer shift δ = 0.30 mm·s^{-1} and quadrupole splitting (Eq) of 0.69 mm·s^{-1}, attributed to Fe^{3+} in octahedral coordination (W=27(1)%). The Fe-ZSM-5 (17) spectrum was decomposed into two doublets, assigned to tetrahedrally (δ = 0.28 mm·s^{-1}, W=83(12) %) and octahedrally coordinated Fe^{3+} (δ = 0.46 mm·s^{-1}, W=17(2)%). The low value of quadrupole splitting (Eq = 0.84 mm·s^{-1}) of tetrahedrally coordinated Fe^{3+}species highlights a more symmetric environment, likely due to the hydrated state of Fe-ZSM-5 zeolite under ambient conditions, as suggested in previous ^{57}Fe Mössbauer spectroscopy studies[47]. Charge-compensating protons are likely incorporated into hydroxonium ions, and the environment surrounding Fe^{3+} is less distorted in the zeolite.

The Mössbauer spectrum of Fe_2O_3/S-1 displayed 3 contributions. The major contribution (W=82.3(1)%) came from a sextet, which signifies Fe_2O_3 in a magnetically ordered state. The isomer shift, quadrupole splitting, and hyperfine field correspond to the hematite iron oxide phase (α-Fe_2O_3) (Fig. 1**.H**, Table 2), corroborating the results from the XRD analysis (see above). The remaining share was described by two doublets with isomer shifts of δ = 0.55 mm·s^{-1} and δ = 0.17 mm·s^{-1}, corresponding to Fe^{3+} in octahedral (W=8.5(1)%) and tetrahedral (W=9(1) %) environments, respectively. The precise configuration of these tetrahedrally coordinated species may be unclear, but their attribution to tetrahedrally coordinated framework Fe^{3+} species (characterized by isomer shift in the range of 0.23 – 0.28 mms^{-1}) can be ruled out, as inferred from the low isomer shift value (Table 2) [26,46,47], absence of Brønsted acid sites (see Table 1**, Figure S5, SI**), and synthesis procedure. Even though a small share of aluminum atoms was detected by ICP-MS in Silicalite-1 (Si/Al = 380, Table 1), our detailed FTIR analysis followed by adsorption of the pyridine probe molecule revealed that neither the parent Silicalite-1 nor the iron-impregnated Fe_2O_3/S-1 contained a significant amount of Al-induced acid sites. Therefore, no iron is found in charge-compensating cationic positions. FTIR studies of pyridine adsorption suggest that these isolated tetrahedral Fe species (observed by ^{57}Fe Mössbauer spectroscopy and DR-UV–vis) are associated with silanol defects of the silicalite-1 zeolite (see py-FTIR discussion below and comment to **Figure S5** in **SI**) [48].

The type (Brønsted/Lewis) and fraction of "strong" (able to protonate/coordinate pyridine at high temperatures) Fe acid sites were analyzed by FTIR spectroscopy of adsorbed pyridine [49,50]. The concentration of Brønsted and Lewis acid sites determined at 150 °C provides information on the total concentration of acid sites (here associated with various Fe-species) of the zeolite (see Table 1, **Figure S6, SI**). But while Brønsted acid sites are attributed to tetrahedrally coordinated framework Fe^{3+} species (Si-OH-Fe) [27], Lewis acid sites can be associated with both coordinatively unsaturated framework-associated Fe^{3+} species and extra-framework iron species in cationic positions [14]. Moreover, the FTIR studies of pyridine adsorption were performed under vacuum and after treatment at high temperatures, whereas the ^{57}Fe Mössbauer spectroscopy was conducted under ambient conditions (and with the zeolite in a hydrated state), complicating our efforts to correlate Fe-species using these techniques. Nevertheless, earlier ^{57}Fe Mössbauer spectroscopy studies of Fe-ZSM-5 have indicated that two tetrahedral components (with varying QS values and IS<0.3 mm·s^{-1}) become apparent in the spectrum upon in-situ evacuation and heating [46,47]. By contrast, under ambient conditions, only one type of tetrahedral and a minor octahedral Fe^{3+} species are observed, as corroborated by our findings. In the hydrated state, coordinatively unsaturated framework-associated [$FeO_{3/2}$] defective species may maintain tetrahedral symmetry to some extent. Therefore, we hypothesize that tetrahedrally coordinated Fe^{3+} species identified by ^{57}Fe Mössbauer spectroscopy under ambient conditions likely contribute to both Brønsted and Lewis acidity assessed by py-FTIR spectroscopy.

Initiating paraffin cracking at 500 °C (formation of primary carbonium/carbenium ions) requires "strong" (Brønsted/Lewis) acid sites [51,52], so we assessed the strength of iron-induced acid sites in the Fe-ZSM-5 catalysts. Here, "strong" acid sites were defined as those able to coordinate or protonate a pyridine molecule at high temperatures. The share of Brønsted and Lewis acid sites was also assessed after pyridine desorption at 250, 350, and 450 °C (Table 1, **Table S1**, **Figure S6-S10**, **SI**). However, during our py-FTIR studies of samples with a higher iron content, Fe-ZSM-5 (17, 21), at 350 and 450 °C, an additional band evolved at 1469 cm^{-1} (see **Figure S8, S9**, **SI**), overlapping with the

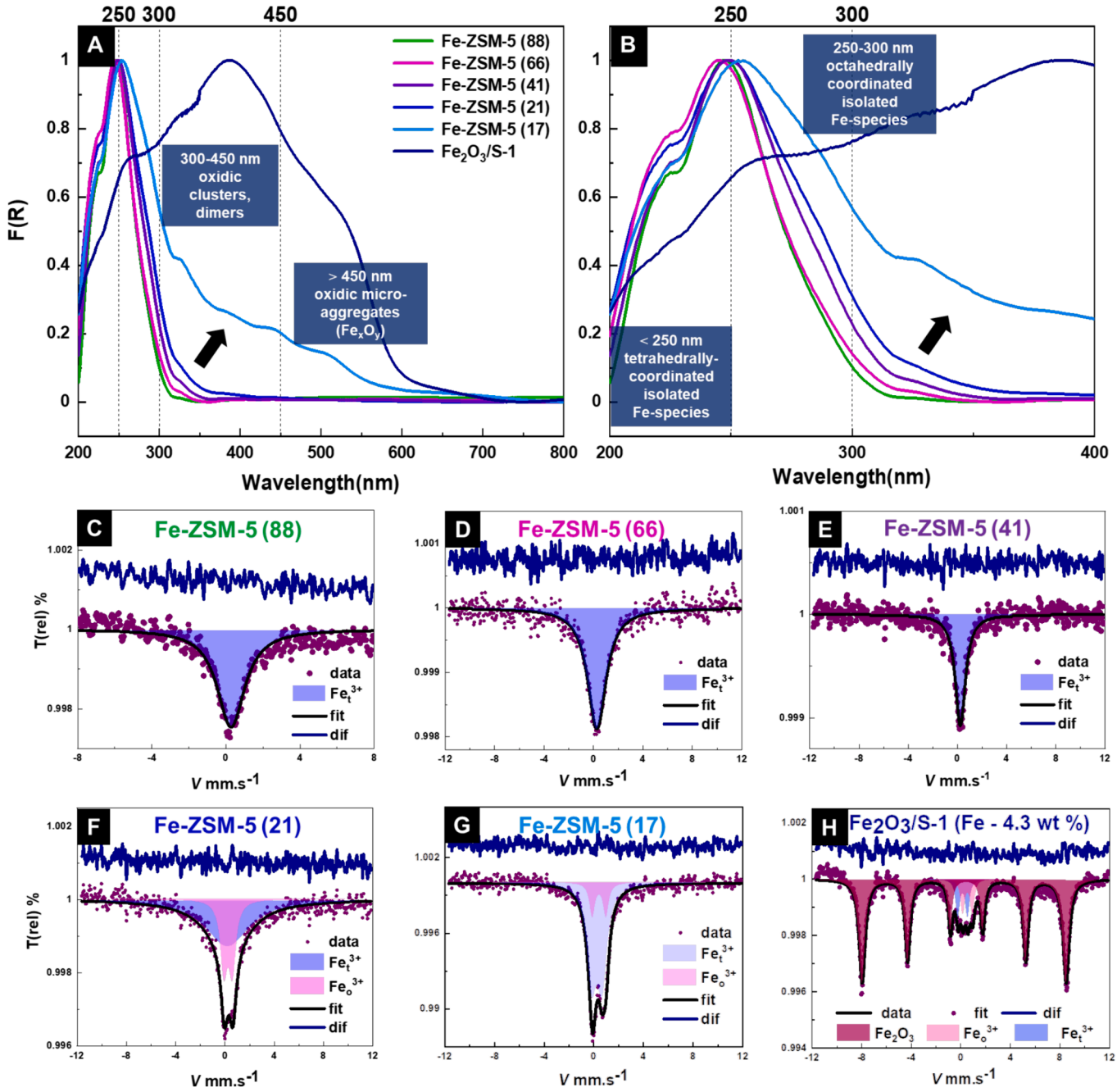

Fig. 1. Characteriation of Fe-species in Fe-ZSM-5 and Fe_2O_3/S-1 zeolites under ambient conditions. A. UV–vis spectra of Fe-ZSM-5 and Fe_2O_3/S-1. **B.** Magnified region of the UV–vis spectra between 200 and 400 nm. **C-H** ^{57}Fe Mössbauer Spectra of Fe-ZSM-5 and Fe_2O_3/S-1. The purple points, black and blue lines correspond to the measured data, fit and residual, respectively.

1455 cm^{-1} band characteristic of the PyL adduct and, thus, suggesting pyridine transformation. Such pyridine transformation at relatively low temperatures has already been reported in prior in-situ XPS (above 70 °C) [53] and infrared (above 150 °C) [54] studies of pyridine adsorption/desorption on α-Fe_2O_3 (hematite). In particular, the infrared study [54] indicated that this pyridine transformation occurs without pyridine ring opening, most likely due to tetrahedrally and octahedrally coordinated Fe cations (of Lewis character) located on the hematite surface (ideally octahedral "corundum" structure). Such defective/coordinatively unsaturated cationic sites should be formed during hematite activation (high temperature and vacuum), which is required for adsorption of the probe molecule (pyridine).

The hematite phase was detected in Fe_2O_3/S-1 (see XRD, ^{57}Fe Mössbauer spectroscopy, **Figure S2**, Fig. 1.**H**, Table 2), but no acid sites (note: the bands at 1444 and 1596 cm^{-1} correspond to hydrogen-bonded pyridine, not Lewis acid sites) [55,56] or pyridine transformation (no additional band at 1469 cm^{-1}) were observed in this sample (see **Figure S5**, **SI**). Moreover, the py-FTIR study of silicalite-1 and impregnated Fe_2O_3/S-1 revealed that isolated tetrahedral Fe cations observed in Fe_2O_3/S-1 (by UV–vis and ^{57}Fe Mössbauer Spectroscopy in Fe_2O_3/S-1, Fig. 1, Table 2) are attributed to unstable Fe ions bound to defective silanol groups of silicalite-1 support (for details, see comment to **Figure S5** in **SI**). In any event, the absence of this band in Fe_2O_3/S-1 spectra suggests that these defective isolated Fe species are either non-acidic or somehow hindered by Fe oxide particles on the zeolite surface, so pyridine is not transformed. Based on these findings, pyridine

Table 2
Summary of values of isomer shift (δ), quadrupole splitting (E_Q), hyperfine field (Bhf), and spectral contribution of the corresponding iron state (w) of all Fe-ZSM-5 samples, Fe_2O_3/S-1, and total Fe wt. % calculated from the ICP-MS measurement.

Sample	Fe state	δ ($mm·s^{-1}$)	E_Q ($mm·s^{-1}$)	B_{hf} (T)	Spectral contribution (%)	Fe wt % (ICP-MS)
Fe-ZSM-5 (88)	Fe_t^{3+}	0.27			100 %	0.7 %
Fe-ZSM-5 (66)	Fe_t^{3+}	0.27			100 %	1 %
Fe-ZSM-5 (41)	Fe_t^{3+}	0.24			100 %	1.6 %
Fe-ZSM-5 (21)	Fe_t^{3+} Fe_o^{3+}	0.230.30	−0.69		73(2) %27(1) %	3.1 %
Fe-ZSM-5 (17)	Fe_t^{3+} Fe_o^{3+}	0.280.46	0.841.10		83(12) %17 (2) %	3.6 %
Fe_2O_3/S-1 (Fe − 4.3 wt %)	α-Fe_2O_3 Fe_o^{3+} Fe_t^{3+}	0.37 0.55 0.17	−0.20 0.76 0.78	51.14	82.3(1)% 8.5(1) % 9(1) %	4.3 %

transformation requires defective/ coordinatively unsaturated iron-induced Lewis acid sites located, e.g., in defective but not ideal α-Fe_2O_3.

The appearance of the 1469 cm^{-1} band in spectra of Fe-ZSM-5 (17, 21) samples indicates that these materials contain more types of Fe-induced Lewis acid sites (likely coordinatively unsaturated framework-associated Fe^{3+} and extra-framework Fe species in cation positions). This result is also in line with the observation that increasing the Fe content decreases the efficiency of iron incorporation into the zeolite framework. Considering the above, the concentration of Lewis acid sites at 450 °C was evaluated from a deconvoluted band at 1455 cm^{-1}, corresponding to the non-transformed Py on those sites.

In summary, in Fe-ZSM-5, iron is identified as major tetrahedrally coordinated framework and framework-associated species (responsible for Brønsted and Lewis acid sites) and minor octahedrally coordinated extra-framework species in the form of oxidic Fe clusters, and oxidic microaggregates. Fe-ZSM-5 samples with high Si/Fe ratios (41, 55, 88) have a higher relative content of "strong" Brønsted acid sites (able to protonate pyridine at higher temperatures) than those with Si/Fe = 17, 21, 28. These data support the observation that increasing the Fe content decreases the efficiency of Fe incorporation into the zeolite framework. Lewis acid sites of Fe-ZSM-5 were still able to coordinate pyridine after desorption at 450℃ across all Fe-ZSM-5 catalysts, whereas all pyridine was released from Brønsted acid sites. Furthermore, pyridine transformation (without ring opening) was observed at higher temperatures (above 250 °C) in Fe-ZSM-5 samples with a high Fe content (Si/Fe = 17, 21), indicating that these materials contain more than one type of strong Lewis acid sites associated with different Fe species (likely coordinatively unsaturated framework-associated Fe^{3+} and extra-framework Fe species in cation positions). When analyzing Fe_2O_3/S-1 prepared by impregnation, we found that most Fe in this sample occurs in the form of α-Fe_2O_3 (hematite), while the remaining share is detected as tetrahedrally and octahedrally coordinated Fe^{3+} species bonded to silanol defects of the silicalite-1 support. This set of Fe-ZSM-5 catalysts containing Fe-species in various concentrations and forms was used to assess their effect on paraffin cracking.

3.2. Acidity of Fe-zeolites vs. Paraffin cracking activity

The contribution of different Fe species of Fe-ZSM-5 to hydrocarbon cracking was studied by gas phase n-octane cracking at 500 °C. This reaction temperature was selected to ensure moderate conversion without severe catalyst deactivation during the 300-min TOS catalytic runs in a fixed-bed reactor. Blank experiments with 2 g of inert SiC ("blank reactor" with the same reactor residence time as that of zeolites) and pure Silicalite-1 (S-1, no acidity, see Table 1, **Figure S5, SI**) were performed for 200 min time-on-stream (TOS). In both cases, the results showed values lower than 1 wt% n-octane conversion (**Figure S11.A, SI.**). The very low yield of mainly C_1-C_5 hydrocarbons was attributed to thermal (non-catalytic) cracking. Similarly, n-octane conversion and the total hydrocarbon yield over the reference Fe_2O_3/S-1 (Fe − 4.3 wt%) was also below 1%, similar to the blank experiments (**Figure S11.A and B, SI;** Fig. 2**. A).** In conclusion, bulk Fe_2O_3 does not catalyze n-octane cracking.

Fig. 2A n-octane conversion over Fe-ZSM-5 and Fe_2O_3/S-1 versus TOS at WHSV=$2h^{-1}$; in hydrothermally synthesized Fe-ZSM-5 catalysts, conversion drops from the initial point (TOS=30 mins), subsequently reaching a steady state. For further comparison, the yields of hydrogen and hydrocarbons were interpolated at 100 mins TOS to assess all Fe-catalysts tested after reaching the steady-state mode (Fig. 2.B.**). n-Octane conversion over Fe-ZSM-5 increased with the Fe content (decreasing Si/Fe molar ratio) and with the overall concentration of acid sites in this series of catalysts. As for the final product distribution, the yield of the C_3-C_4 fraction (also known as liquid petroleum gas, LPG) was the highest of all products (Fig. 2**.B.**, **Table S2, SI**), showing an overall selectivity to LPG of 50–64% (see **Table S2, SI**). Moreover, C_3 and C_4 olefinicity (individual selectivity to olefins within each carbon number fraction) reached 80–85% (see **Table S2, SI**).

Considering the reaction mechanism, the occurring transformations can be divided into 3 groups: a) primary paraffin cracking; b) olefin oligomerization/aromatization, and c) unsaturated oligomers re-cracking. Among them, primary cracking, which requires paraffin activation, determines the n-octane conversion rate and has the highest activation energy [57] (disregarding paraffin dehydrogenation activation energy, which is higher). Thus, the reaction initiation step is the most important step.

Multiple studies on hydrocarbon cracking over aluminosilicate zeolites have shown that catalytic activity is associated with the concentration and strength of Brønsted and Lewis acid sites in these materials [51,52,58]. Considering that paraffin cracking initiation requires "strong" acid sites, we correlated n-octane conversion over the Fe-ZSM-5 and Fe_2O_3/S-1 at TOS=30 mins vs. the number of "strong" Brønsted and Lewis acid sites, defined here as acid sites, which can still protonate and/or coordinate pyridine at a pyridine desorption temperature of 450 °C (Fig. 2**.E. and F**). Our Fe-ZSM-5 is compared with Al-ZSM-5 in **Section 3.3**.

From a mechanistic standpoint, two key reaction pathways are considered in the initiation of paraffin cracking over aluminosilicate zeolite catalysts: i) the carbonium ion mechanism (paraffin protonation, forming a penta-coordinated carbon atom) by Haag-Dessau [52] and (ii) the classical carbenium ion pathway [51]. The Haag-Dessau mechanism, also known as protolytic or monomolecular cracking, is based on direct protonation of the paraffin C-C or C-H bond. This protonation has a very high activation energy [59] and, hence, demands very strong Brønsted acid sites (similar to those of superacids), which can be found in fresh (non-equilibrated) H^+-Al-ZSM-5 [60]. In Fe-zeolites, superacidity is improbable because their Fe^{3+} generated acid sites are weaker than those of Al^{3+} [61,62]. Therefore, direct paraffin protonation is highly unlikely a prevalent reaction path.

Carbenium ions are generated by protonation of olefins in the feed (not the case here) or olefin products of thermal cracking, or by hydride abstraction from paraffins on Lewis acid sites. Subsequently, the carbenium ions are cracked via ß-scission, yielding (upon hydride abstraction from paraffin) an olefin and paraffin fragments. In Fe-ZSM-5 zeolites, the Lewis acid sites were able to coordinate pyridine at 450 °C, while Brønsted acid sites were no longer able to protonate pyridine (see concentration after pyridine desorption at 450℃, Table 1, **Figure S6, SI**). So, the most realistic initiation step of the n-octane (paraffin) cracking over an Fe-zeolite is via carbenium ion formation on Lewis acid sites.

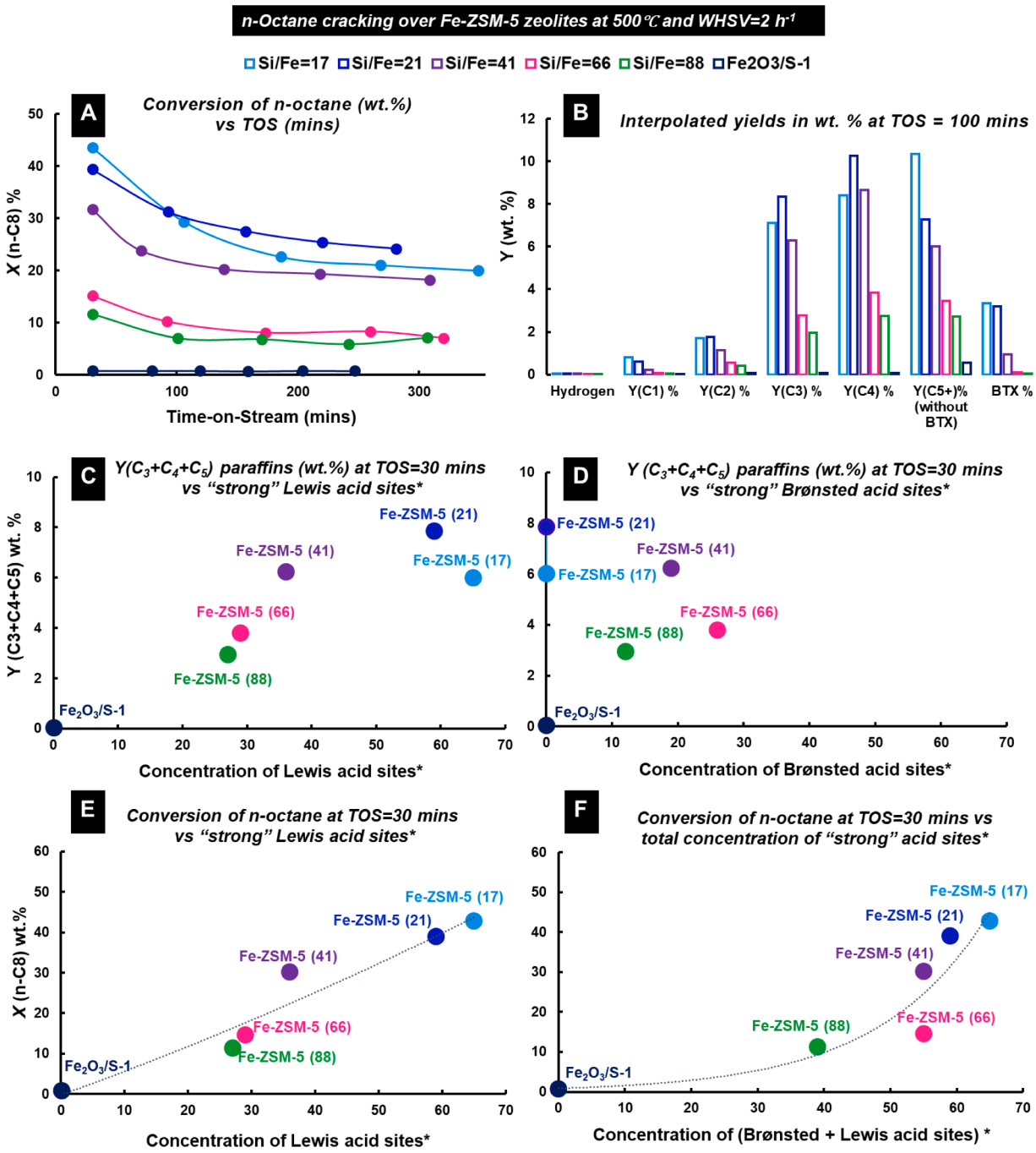

Fig. 2. Paraffin cracking activity vs Fe-zeolites acidity. A. Conversion (wt.%) of n-octane over Fe-ZSM-5 zeolites and Fe_2O_3/S-1 vs TOS (mins) at 500℃ and WHSV=2h^{-1}**B.** Interpolated yields of n-C_8 cracking products at TOS=100 mins **C.** Yield of C_3 + C_4 + C_5 paraffins ("terminal products") at TOS=30 mins vs the concentration of Lewis acid sites (in μmol pyridine/g at pyridine desorption at 450 °C) **D.** Yield of C_3 + C_4 + C_5 paraffins ("terminal products") at TOS=30 mins vs the concentration of Brønsted acid sites (in μmol pyridine/g at pyridine desorption at 450 °C) **E.** Conversion of n-C_8 at TOS=30 mins vs the concentration of Lewis acid sites (in μmol pyridine/g at pyridine desorption at 450 °C) **F.** Conversion of n-C_8 at TOS=30 mins vs the total concentration of Brønsted and Lewis acid sites (in μmol PY/g at pyridine desorption at 450 °C).

Assuming that n-octane cracking over Fe-zeolites is initiated on Lewis acid sites, C_3, C_4 and C_5 paraffins and olefins will be the initial products of cracking by ß-scission. Conversely, C_1 and C_2 paraffins will unlikely be formed by this mechanism given the high instability of C_1 and C_2 carbenium fragments. Unsurprisingly, C_1-C_2 are usually formed via a radical mechanism (e.g., thermal cracking). While C_3-C_5 olefins may further participate in isomerization, oligomerization, and hydrogen transfer reactions [63], the respective C_3-C_5 paraffins should be terminal products (not further transformed) and, thus, reflect the initial cracking step, based on the knowledge on paraffin cracking over Al-ZSM-5.

Accordingly, the total yield of C_3, C_4, and C_5 paraffins should depend on the concentration of the Lewis acid sites responsible for the initiation reaction. Fig. 2.**C.** shows the total C_3, C_4, C_5 paraffin yield (at TOS=30 mins) of all Fe-ZSM-5 samples and Fe_2O_3/S-1 plotted against the number

of "strong" Lewis acid sites, defined here as sites which maintain pyridine after desorption at 450 °C. The yield of C_3, C_4, C_5 paraffins over Fe-ZSM-5 catalysts increases with the concentration of Lewis acid sites until it peaks for Si/Fe = 21 and then drops for Si/Fe = 17. Brønsted acid sites with adsorbed pyridine at 450 °C were either not observed (for Fe-ZSM-5 (17, 21)) or their concentration was low (Fe-ZSM-5 (41, 66, 88)) in all Fe-ZSM-5 zeolites under study, whereas n-octane conversion and C_3, C_4, C_5 paraffin formation continued, in line with the aforementioned initiation mechanism (Fig. 2**.D.**). Fe_2O_3/S-1 was also inactive, as expected, given the lack of acidity (evidenced by pyridine adsorption) of the iron oxide phase and iron cations associated with Si-OH defects (see Table 1, **Figure S5**). These results show that Lewis acid sites strong enough to initiate cracking are framework-associated Fe^{3+} species (coordinatively unsaturated Fe^{3+} sites**).** n-Octane conversion correlated well with the total number of acid sites at 450°C (Fig. 2**.F)** along with the small share of Brønsted acid sites (Fig. 2**.D.**) detected in Fe-ZSM-5 (Si/Fe = 41, 66, 88). So, Brønsted and Lewis acid sites responsible for n-octane cracking initiation over these catalysts may have a cooperative effect. However, initiation on Lewis acid sites (carbenium ion formation) should prevail (Fig. 2**.E**) since the Lewis acid sites of Fe-ZSM-5 catalysts prevail over their Brønsted counterparts at high temperatures (Table 1, **Figure S6, SI**). Therefore, n-octane cracking initiation over Fe-ZSM-5 catalysts requires strong framework associated (coordinatively unsaturated) Fe^{3+} induced Lewis acid sites, which can abstract hydride from paraffin and form the primary carbenium ion.

3.3. Comparison of Fe-ZSM-5 vs. Al-ZSM-5

When comparing the contribution of Fe-species to the catalytic activity and product distribution of Fe-ZSM-5 (Si/Fe = 17,21) zeolites with those of their Al-ZSM-5 (Si/Al = 25,60) analogs, we found that the samples showed comparable textural properties (Table 1) and a crystal size of approximately 0.3 μm, except for Al-ZSM-5 (60) with 4–6 μm (**Figure S12**, SI). Under these conditions, differences in catalytic properties among Fe-ZSM-5 (17), Fe-ZSM-5 (21), and Al-ZSM-5 (25) can be ascribed exclusively to differences in active sites. Any comparison with Al-ZSM-5 (60) is slightly more complex, but the larger crystals should decrease the catalytic activity by lengthening the diffusion pathway.

The experimental conditions (WHSV) of the catalytic tests were adjusted to similar n-octane conversion values (of approximately 30%, Fig. 3**.A**, Table 3). This adjustment was necessary because some catalysts were more active than others, particularly Al-ZSM-5 (25), over which conversion reached 90% at WHSV=14 h^{-1} (30 min TOS, not shown), in contrast to ~ 40% at WHSV=2h^{-1} over Fe-ZSM-5 (17) and Fe-ZSM-5 (21) at 30 mins TOS. WHSV=122 h^{-1} and 7 h^{-1} were used for Al-ZSM-5 (25) and Al-ZSM-5 (60), respectively (Table 3). Notably, the WHSV 7 h^{-1} needed for Al-ZSM-5 (Si/Al = 60) to provide 30% conversion matches the predicted effect of the larger crystals (WHSV~40 h^{-1} was expected based on the Al content).

The aluminosilicate Al-ZSM-5 (25) is 60-times more active (per unit of catalyst mass) than Fe-ZSM-5 (21), reaching a similar conversion (~30 %, Table 3) at a 60 times higher WHSV=122 h^{-1} than its Fe counterpart (WHSV=2h^{-1}) at 100 mins TOS. This difference supports the hypothesis that Fe^{3+} acid sites are weaker than Al^{3+} acid sites [61,62,64]. Moreover, the Al-ZSM-5 catalysts were more stable than Fe-ZSM-5, as the initial conversion over Al-ZSM-5 (25) only dropped 3% (from 35 to 32%) after 286 mins TOS, while over Fe-ZSM-5 (21) conversion decreased 15% (from 39 to 24%) after 281 mins TOS (Fig. 3**.A.**).

The amount of coke accumulated on Fe-ZSM-5 (17,21) and Al-ZSM-5 (25,60) was determined by thermogravimetric analysis (TGA) of "spent" (after 1 cracking cycle) catalysts (see **Table S3**, ***Eq. S1-Eq. S5***, SI). TGA weight loss (***$m_{coke\ TGA}$, SI***) above 400 °C [65] up to 750 °C (attributed to coke combustion under airflow) was used as a measure of the overall weight of coke formed on the catalyst during the cracking test. All Fe- and Al-ZSM-5 samples contained less than 2 wt% of coke on the catalyst after the cracking test (TOS 281–349 mins, see **Table S3**). Al-ZSM-5 (25)

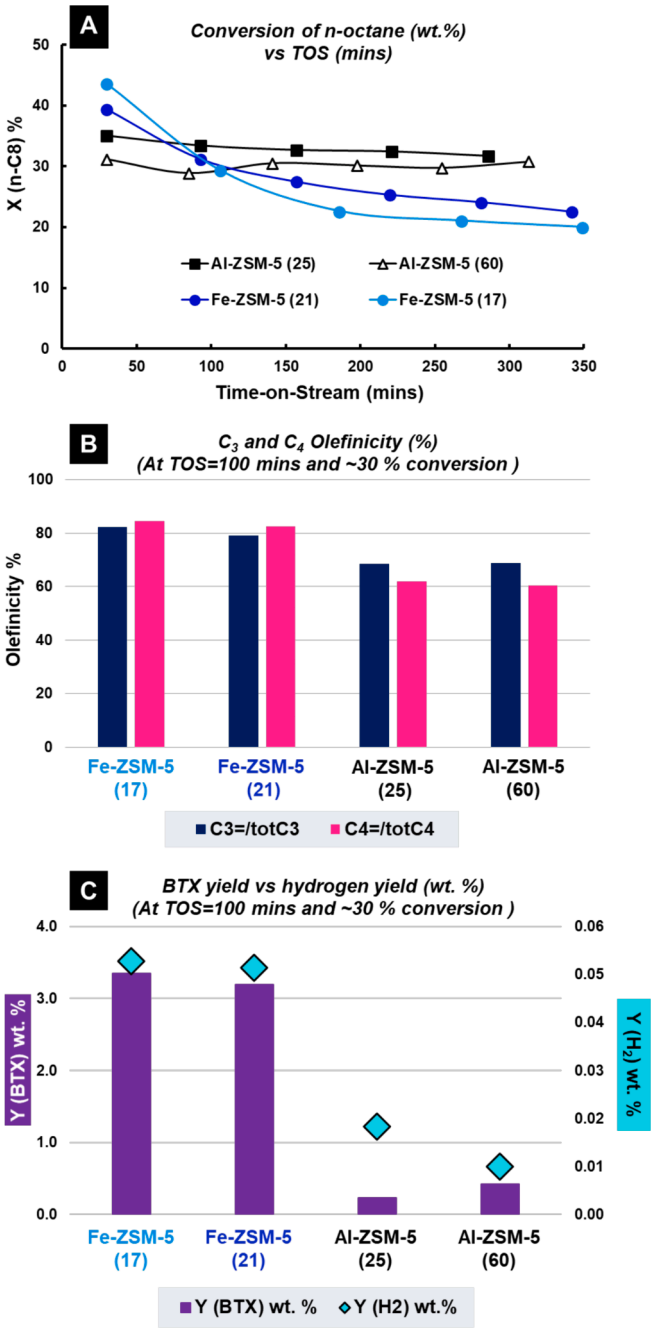

Fig. 3. Fe-ZSM-5 vs Al-ZSM-5 in n-octane cracking. A Conversion of n-octane (wt.%) vs. TOS (mins) over Fe-ZSM-5 (17, 21) and Al-ZSM-5 (25, 60) **B.** C_3,C_4 Olefinicity (%) and **C.** BTX vs hydrogen yield (wt.%) at TOS=100 mins and ~ 30% conversion for Fe-ZSM-5 (17,21) and Al-ZSM-5 (25,60).

had the highest coke content (1.91 wt%), in line with its concentration of acid sites (see **Figure S6**, **Table S1**) and catalytic activity, which were also the highest. The Al-free ferrisilicate analog Fe-ZSM-5 (21) contained 1.1 wt%. For each catalyst, the amount of coke was also re-calculated to wt.% of feed (<0.12 wt%; see **coke $_{wt.\%\ F}$**, **Table S3**). Coke species were not analyzed because they were outside the scope of this study.

Table 3 shows the product distribution (yields in wt.% at TOS=100 mins) over the two types of catalysts. Methane, ethane, and ethene (dry gas) are generally formed by thermal or metal-assisted (in the presence of metal promoters in zeolites) cracking via a radical formation or protolytic cracking mechanism [52,66]. In our case, the yield of the C_2 fraction was higher over Al-ZSM-5 (25, 60) than over Fe-ZSM-5, possibly

Table 3
Comparison of Fe-ZSM-5 (17, 21) and Al-ZSM-5 (25, 60) catalysts in n-octane cracking at 500 °C and 100 mins Time-on-Stream.

	Fe-ZSM-5 (17)	Fe-ZSM-5 (21)	Al-ZSM-5 (25)	Al-ZSM-5 (60)
WHSV (h^{-1})	2	2	122	7
Conversion (%)	31.6	31.4	33.6	30.2
Hydrogen (wt. %)	0.05	0.05	0.02	0.01
Yield (C_1 wt. %)	0.80	0.62	0.18	0.23
Yield (C_2 wt. %)	1.69	1.76	4.42	3.80
Yield (C_3 wt. %)	7.10	8.35	13.82	11.49
Yield (C_4 wt. %)	8.39	10.25	10.31	9.06
Yield BTX (wt. %)	3.35	3.19	0.23	0.42
Yield C_{5+} excl. BTX (wt. %)	10.3	7.26	4.71	5.20
LPG olefinicity (%)	83.50	80.86	65.71	65.06
C_3 olefinicity (%)	82.30	78.90	68.57	68.82
C_4 olefinicity (%)	84.52	82.45	61.88	60.28

due to the protolytic cracking on the "strong" Brønsted acid sites in the fresh aluminosilicate zeolites [52,60,66]. This explanation is supported by the higher concentration of strong Brønsted acid sites in Al-ZSM-5 than in Fe-ZSM-5 at a pyridine desorption temperature of 450 ℃ (Table 1, **Figure S6**, **Figure S10**, **SI**).

The yield of the C_3-C_4 fraction was higher over Al-ZSM-5 catalysts (20–24 wt%) than over Fe-ZSM-5 (15–18 wt%) catalysts; nevertheless, C_3-C_4 olefinicity (the share of olefins in the whole fraction) was higher over Fe-catalysts, (80–83 %), reaching only 65% over their Al counterparts (Fig. 3**.A,** Table 3**).** As discussed above, over Al-ZSM-5, C_3-C_5 paraffins are likely terminal products of C_8-paraffin cracking (via Lewis acid sites activation and further ß-scission), whereas primarily formed olefins participate in subsequent oligomerization and aromatization reactions. However, previous studies have suggested that iron-silicate catalysts have more dehydrogenation properties than aluminosilicates [37]. If our Fe-zeolites catalyzed dehydrogenation, then C_3, C_4, and C_5 paraffins would not be the terminal products.

Considering the above, we investigated the contribution of Fe-ZSM-5 dehydrogenation activity to propane dehydrogenation. Fe-ZSM-5 (28), Fe_2O_3/S-1, and Al-ZSM-5 (25) were tested at 500 °C (same as for the n-octane cracking; **Figure S13**, **SI**). The amount of Fe-ZSM-5 (28) and Fe_2O_3/S-1 was the same as that used in the n-octane cracking tests, but the amount of Al-ZSM-5 (25) was adjusted to match the conversion (~2%) over Fe-ZSM-5 (28) (**Figure S13.A, SI**). Fe-ZSM-5 (28) was 97% selective to propene formation (dehydrogenation), while Al-ZSM-5 (25) provided only 27% selectivity to C_3H_6. In addition to propene formation, Al-ZSM-5 (25) also catalyzed cracking to ethene (48 %) and methane (25%), corroborating the findings of a previous study [37] (**Figure S13. B, SI**). Fe_2O_3/S-1 was inactive, showing less than 1% C_3H_8 conversion (as in the blank experiment, see **Figure S13.A**, **SI**). The most notable result was the overall conversion of propane (2%) over Fe-ZSM-5 (28) using 600 mg of catalyst 500℃, as in the cracking experiments. In other words, direct dehydrogenation of propane (n-octane cracking product) does not significantly increase C_3 olefinicity over Fe-ZSM-5. Therefore, propane is indeed a terminal product.

The higher C_3-C_4 olefinicity over Fe-ZSM-5 catalysts was not fully explained either by the initial preferential formation of C_{5+} olefins and their further oligomerization and re-cracking over Fe-induced acid sites. Even in the extreme case of maximum overall olefin selectivity (62.5%) at the initial n-octane cracking step to propane and pentene products, the total C_3-C_5 paraffin yield at 31.4% conversion for Fe-ZSM-5 (21) would be 11.8%. However, the observed yield of C_3-C_5 paraffins over Fe-ZSM-5 (21) was only 5.93% (see 100 min TOS, Table 3, Fig. 3). This lower yield of n-paraffins could only be explained by dehydrogenation. Therefore, higher paraffins must have a stronger contribution to dehydrogenation, albeit impossible to track (particularly for C_{5+} paraffins) due to parallel cracking of the C_{5+} olefins formed by dehydrogenation.

In addition to increased olefinicity, the yield of the highly valuable benzene-toluene-xylene (BTX) fraction was an order of magnitude higher over Fe-ZSM-5 (3.2–3.5 wt%) than over Al-ZSM-5 (0.23–0.42 wt %). This fraction is a marker of aromatization reactions, a multistep sequence that includes oligomerization of olefins, cyclization, and dehydrogenation. Generally, the olefin aromatization pathway is promoted by the presence of Brønsted acid sites [67,68] and metal species [69] in zeolites. As such, the Brønsted acid sites of the Fe-ZSM-5 may be strong enough to catalyze the oligomerization/aromatization, but not the re-cracking of intermediate precursors to aromatics, such as oligomers and cycloparaffins, in contrast to the Al-ZSM-5, thus accounting for the higher BTX yield over these catalysts. This hypothesis is also supported by the higher yield of oligomers observed in this study (see C_{5+} yields, Table 3). Furthermore, the dehydrogenation properties of Fe species likely play a role in the conversion of cycloparaffin products to BTX, and aromatization also explains the higher yield of hydrogen gas over Fe-ZSM-5 samples vs. Al-ZSM-5. So, while Fe-ZSM-5 zeolites are less active (require much lower WHSV to reach similar conversion rates) and less stable (higher conversion drop) than their Al-ZSM-5 counterparts under cracking conditions, they significantly increase the olefinicity of the highly valuable C_3-C_4 fraction (via oligomerization and re-cracking) and the yield of the BTX mixture (via aromatization). Undoubtedly, the real industrial FCC unit operation will require using both REUSY and the introduction of both Fe and Al into the ZSM-5 additive, maing it possible to reach desirable conversion while increasing selectivity levels.

3.4. Deactivation study of Fe-ZSM-5 catalysts

The stability of Fe-ZSM-5 catalysts was evaluated by *in-situ* regeneration, catalytic testing, and spent catalyst characterization of the Fe-ZSM-5 (28) sample. After a catalytic run of 300 min TOS, the catalyst was *in-situ* regenerated under synthetic airflow (60 ml/min) overnight at 500 °C and subjected to another run. This cycle was repeated twice without removing the catalyst from the reactor. The purpose of these in-situ regenerations was not to age the catalyst further between runs but simply to remove coke in order to run another cracking cycle "on the same catalyst." In the first run, the catalyst underwent a rapid initial deactivation (conversion dropped from 35 to 22%). In the 2nd and 3rd cycles, the initial activity was not restored but the catalyst provided an equilibrated conversion value between 18 and 23%, which dropped only slightly during the run and was restored upon regeneration between the 2nd and 3rd cycle (Fig. 4**.A**). Although the total yield of the C_3-C_4 fraction decreased with each cycle (along with conversion), the olefinicity of the C_3 and C_4 fractions (selectivity to propene or butenes) and BTX yield increased with each cycle (Fig. 4**.B**).

To interpret such catalytic behavior, the Fe-ZSM-5 (28) catalyst characterized in "calcined" (sample before cracking tests), "spent" (in a coked state after 3 cracking cycles), and "regenerated" (after 3 cracking cycles) states. X-ray diffraction analysis revealed that Fe-ZSM-5 preserves its structure without losing crystallinity after 3 cycles of cracking and in-situ regenerations (**Figure S14**, **SI**). No difference in textural properties or isotherm shapes was observed between the "calcined" and "regenerated" states of the catalyst (**Figure S15**, **Table S4**, **SI**). Based on these results, the "permanent deactivation" observed between the 1st and 2nd cycle is not caused by blocked catalyst pores and, therefore, likely results from a transformation of active Fe-species.

To identify this transformation, the same set of samples was analyzed by low-temperature ^{57}Fe Mössbauer spectroscopy, DR-UV–Vis spectroscopy, and py-FTIR analysis. Fig. 5 shows Mössbauer Spectra at −269 °C and **Table S5** **(SI)** fitted parameters of Fe-ZSM-5 (28) in all 3 states mentioned above. The spectrum of the "calcined" sample was fitted with two contributions from the "iron-rich" and "iron-poor" Fe^{3+} phases. The "iron-poor" phase contained the well-distributed Fe^{3+} ions with large Fe-Fe distances in the tetrahedral framework (and framework-associated) positions (W=66%), giving rise to a sextet pattern assigned to paramagnetic hyperfine splitting [70]. The "iron-

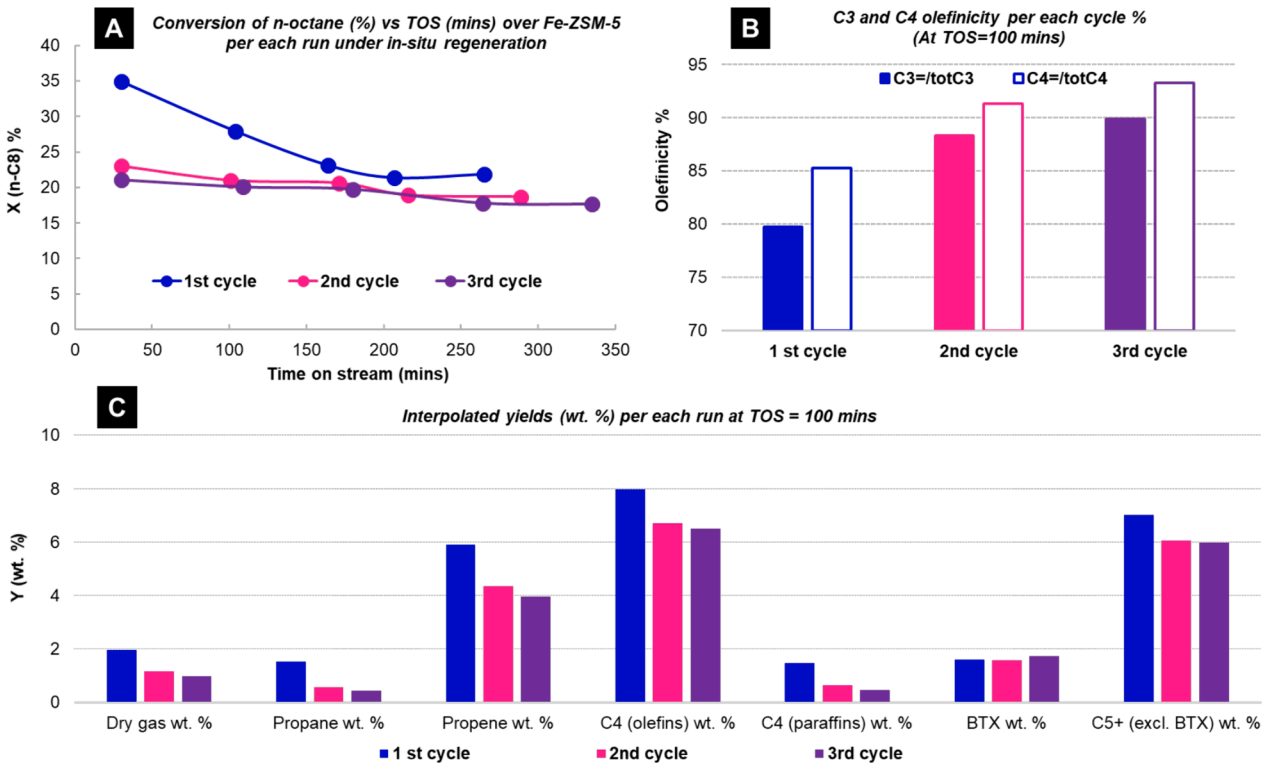

Fig. 4. Fe-ZSM-5 behavior under in-situ regeneration and n-octane cracking at 500 °C. A. Conversion of n-octane over Fe-ZSM-5 (28) in each cycle under in-situ regeneration (under air) **B.** C_3,C_4 olefinicity (%) and **C.** Interpolated yields of hydrocarbon products (wt. %) at TOS=100 mins for each cycle.

rich" phase (W=34%) was assigned to octahedral Fe^{3+} (doublet pattern with large quadrupole splitting) arising from the faster relaxation rates from neighboring iron ions with shorter distances (increased concentration of neighboring Fe atoms), interpreted as extra-framework Fe^{3+} (dimers or small clusters). The isomer shift values at −269 °C (**Table S5, SI**) differ (need to subtract 0.12 mm/s) from the respective iron species at room temperature (Table 2) due to the decreased vibration of Fe atoms at cryogenic temperatures.

In the "spent" sample, the iron-poor phase (sextet) showed an increased isomer shift (0.51 mm/s), which is characteristic of octahedral structures and may be attributed to coked species (extending the coordination of framework Fe-species) or to Fe^{3+} ions which migrated to extra-framework positions. However, upon regeneration, this sextet component showed a reduced isomer shift value (0.37 mm/s) again, indicating restoration of framework or framework-associated tetrahedral Fe^{3+} species. Nevertheless, the amount (spectral contribution) of Fe^{3+} with tetrahedral coordination (44%) was lower than that in the "calcined" sample (66%). Accordingly, upon cracking, Fe-species in Fe-ZSM-5 catalysts may undergo temporary (active sites are blocked by coke) and permanent (migration of Fe ions to extra-framework positions) deactivation.

This interpretation agrees with the results from our DR-UV–vis analysis of the regenerated sample (**Figure S16, SI**), showing additional absorption bands in the 300–500 nm region, which correspond to non-framework Fe^{3+} species in oligomeric clusters and dimers (see DR-UV–vis discussion above). In these samples, changes in the concentration of acid sites were analyzed by py-FTIR. To preserve the effect of coke on the "spent" catalyst, all three samples were analyzed only by pyridine desorption at 150°C (**Table S4, SI).** Concentrations of Brønsted and Lewis acid sites in the "spent" sample decreased significantly because coke blocked these acid sites. The regenerated sample contained more Lewis acid sites than the "calcined" sample at the expense of their Brønsted counterparts due to Fe^{3+} migration from framework to extra-framework positions. The higher concentration of Lewis acid sites in the "regenerated" sample observed at 150 °C is likely associated with the migration of framework-associated Fe^{3+} Lewis acid sites to extra-framework cationic positions. The latter likely have weaker Lewis acid sites than framework-associated ones, which explains the drop in conversion in the 2nd and 3rd cracking cycles.

The rapid initial decrease in conversion over Fe-ZSM-5 catalysts (and hence the hydrocarbon yield as well) is attributed to the loss of tetrahedrally coordinated Fe^{3+} species, which are responsible for the initiation of cracking, as shown by ^{57}Fe Mössbauer analysis (Fig. 5, **Table S5, SI**). Concurrently, the increases in C_3-C_4 olefinicity and BTX yield in the 2nd and 3rd cycles are likely associated with increased shares of extra-framework Fe^{3+}/oxidic micro-aggregate species (see DR-UV–vis, **Figure S16, SI**). Such extra-framework iron species promote dehydrogenation step(s) [37], yielding aromatics (BTX) and dehydrogenating cyclic and branched oligomers and likely even higher (C_5 +) linear paraffins under reaction conditions, explaining the higher product olefinicity observed in the 2nd and 3rd cycles. Therefore, the ultimate goal of tuning the FCC catalyst Fe additive may be achieved by stabilizing the Fe atoms in the catalyst framework while preserving the increased selectivity to the highly valued C_3-C_4 olefins and aromatics by balancing framework and cationic Fe^{3+} species.

4. Conclusions

In n-octane cracking at 500 °C over iron-silicate ZSM-5 catalysts, tetrahedrally coordinated framework-associated Fe^{3+} species, which form strong Lewis acid sites, are the key active species in paraffin cracking initiation. Framework Brønsted acid sites are strong enough to catalyze the aromatization of olefin cracking products to BTX but not the re-cracking of intermediate precursors to aromatics (unlike Al-ZSM-5). The oxidic iron aggregates (Fe_2O_3) on the external surface of these zeolite catalysts are inactive. Dehydrogenation properties of Fe-ZSM-5 promote higher olefinicity and aromatization (unlike Al-ZSM-5). Al-free Fe-ZSM-5 (Si/Fe = 21) are less active than their Fe-free Al-ZSM-5

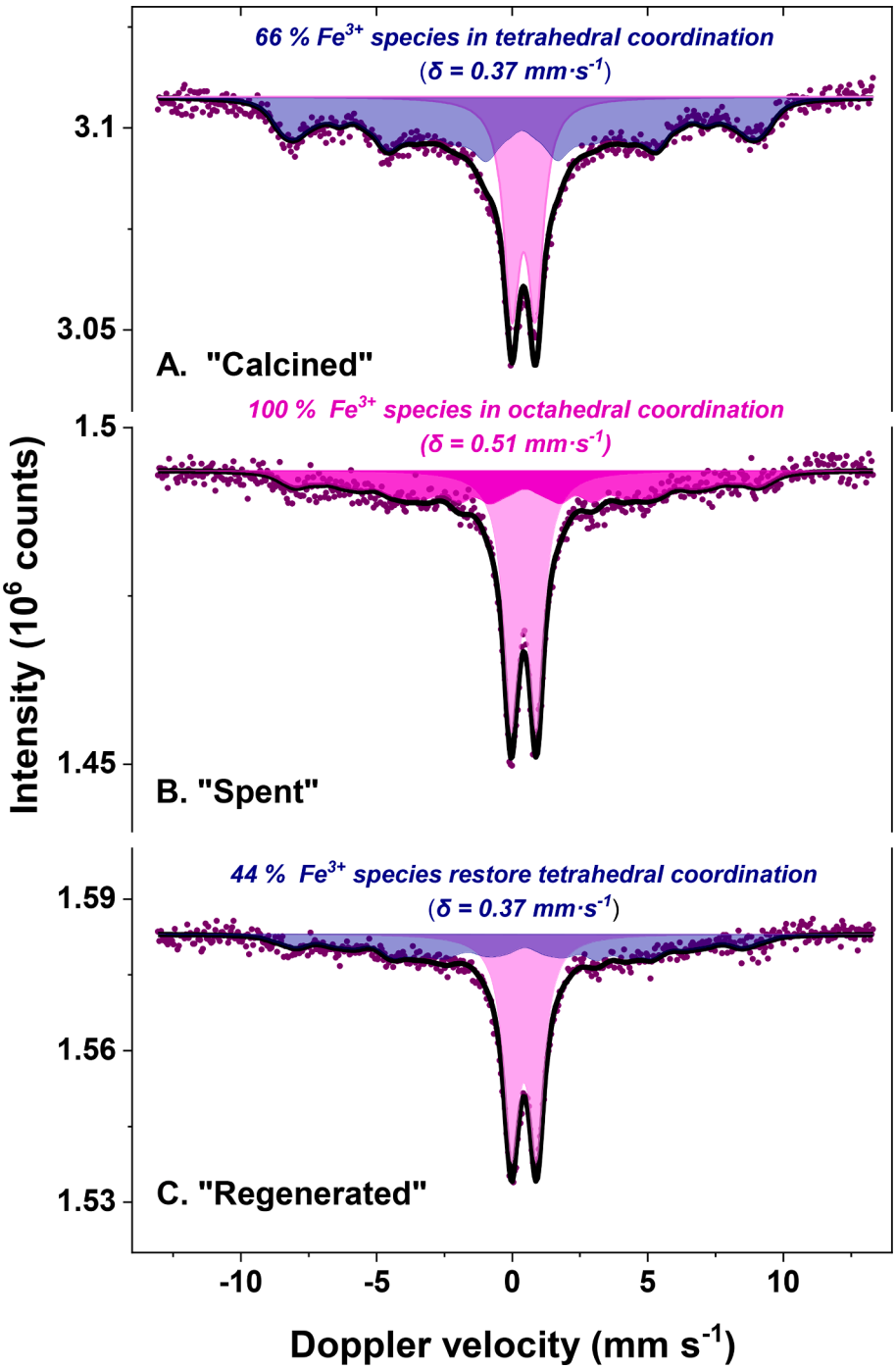

Fig. 5. Transformation of Fe-species in Fe-ZSM-5 under paraffin cracking. ^{57}Fe Mössbauer spectra (obtained at −269 °C) of Fe-ZSM-5 (28) in "calcined," "spent," and "regenerated" states. The purple points, black lines, and blue- and pink-colored spectra correspond to the measured data, fit, tetrahedrally coordinated Fe^{3+} species, and octahedrally coordinated Fe^{3+}, respectively.

(Si/Al = 25) analogs because their iron-induced acid sites are weaker. However, the C_3-C_4 olefinicity (ratio of the yield of olefins to the total yield of a given hydrocarbon fraction) of Fe-ZSM-5 (78–82%) is higher than that of Al-ZSM-5 (61–68%). This difference cannot be fully explained by preferential formation of larger olefin and smaller paraffin in the initial cracking step, so Fe-ZSM-5 catalyzes the dehydrogenation of C_{5+} paraffins. The resulting olefins subsequently undergo oligomerization and re-cracking, yielding more C_3-C_4 olefins than paraffins. Moreover, Fe-ZSM-5 provides a much higher BTX yield (3.2 wt%) than Al-ZSM-5 (0.23 wt%) and accordingly a higher yield of hydrogen (0.05 vs. 0.02 wt%) and C_{5+} (excluding BTX) fractions (7.2 vs. 4.7 wt%). Fe-zeolites undergo permanent deactivation (loss of activity at the beginning of the 1st catalytic test) because tetrahedrally coordinated Fe^{3+} species migrate to extra-framework positions, thereby increasing the concentration of octahedrally coordinated Fe^{3+} species. This increase in extra-framework Fe^{3+} species enhances the olefinicity of C_3-C_4 fractions and the BTX yield (in 2nd and 3rd catalytic cycles), most likely due to their dehydrogenation activity, but these extra-framework Fe^{3+} species do not catalyze dehydrogenation of propane. Therefore, Fe-ZSM-5 FCC catalytic C_3-C_4-selective additives may be tuned by stabilizing framework Brønsted and framework-associated and cationic Lewis acid sites and by minimizing the prevalence of Fe oxide species.

CRediT authorship contribution statement

Anastasia Kurbanova: Writing – original draft, Visualization, Investigation. **Dominika Zákutná:** Resources, Investigation. **Kinga Gołąbek:** Investigation. **Jakub Hraníček:** Investigation. **Achim Iulian Dugulan:** Resources, Investigation. **Paul Diddams:** Writing – review & editing, Methodology, Conceptualization. **Ming-Feng Hsieh:** Supervision, Funding acquisition, Conceptualization. **Nicolas Bats:** Supervision, Funding acquisition, Conceptualization. **Jan Přech:** Writing – review & editing, Supervision, Methodology, Conceptualization.

Declaration of competing interest

The authors declare that they have no known competing financial interests or personal relationships that could have appeared to influence the work reported in this paper.

Data availability

The data that has been used is confidential.

Acknowledgements

The authors thank Dr. Martin Kubů for the N_2 adsorption and ICP-MS analyses, Dr. Daniel Rainer and Emad Shamma for SEM imaging, Petr Golis for the DR-UV-Vis measurements, Associate Prof. Mariya Shamzhy and Dr. Subhajyoti Samanta for py-FTIR measurements of silicalite-1. The authors acknowledge the Viničná Microscopy Core Facility (VMCF of the Faculty of Science, Charles University), which is funded by MEYS CR (LM2023050 Czech-BioImaging), for their support and assistance in this work. The authors also acknowledge the Charles University Centre of Advanced Materials (CUCAM—OP VVV Excellent Research Teams, no. CZ.02.1.01/0.0/0.0/15_003/0000417) for providing instrumental facilities enabling this research. The authors would like to thank Professor Jiří Čejka for his helpful suggestions and content review analysis, as well as Dr. Riho Green, Dr. Veselina Geogieva, Dr. Charles Kanyi, Dr. Luis Murillo, and Dr. Mehdi Allahverdi for their fruitful discussions. The authors also thank Johnson Matthey for their permission to publish their findings and Dr. Carlos V. Melo for editing this manuscript. This research was funded by Johnson Matthey PLC, UK, and by the Ministry of Education, Youth and Sport of the Czech Republic through ERC CZ project LL2104.

Appendix A. Supplementary data

Supplementary data to this article can be found online at https://doi.org/10.1016/j.cej.2024.156032.

References

[1] J. Biswas, I.E. Maxwell, Amsterdam-Printed in The Netherlands 197, Appl. Catal. 63 (1990) 197–258, https://doi.org/10.1016/S0166-9834(00)81716-9.
[2] E.T.C. Vogt, B.M. Weckhuysen, Fluid catalytic cracking: recent developments on the grand old lady of zeolite catalysis, Chem. Soc. Rev. 44 (2015) 7342–7370, https://doi.org/10.1039/c5cs00376h.
[3] A. Oloruntoba, Y. Zhang, C.S. Hsu, State-of-the-Art Review of Fluid Catalytic Cracking (FCC) Catalyst Regeneration Intensification Technologies, 2061, Energies (basel) 15 (6) (2022), https://doi.org/10.3390/en15062061.
[4] T.F. Degnan, G.K. Chitnis, P.H. Schipper, History of ZSM-5 fluid catalytic cracking additive development at Mobil, Microporous Mesoporous Mater. 35 (2000) 245–252, https://doi.org/10.1016/S1387-1811(99)00225-5.
[5] D.S. Stratiev, I.K. Shishkova, D.S. Dobrev, Fluid catalytic cracking feed hydrotreatment and its severity impact on product yields and quality, Fuel Process. Technol. 94 (2012) 16–25, https://doi.org/10.1016/j.fuproc.2011.10.014.
[6] M.A. Alabdullah, A.R. Gomez, J. Vittenet, A. Bendjeriou-Sedjerari, W. Xu, I. A. Abba, J. Gascon, A viewpoint on the refinery of the future: catalyst and process challenges, ACS Catal. 10 (2020) 8131–8140, https://doi.org/10.1021/acscatal.0c02209.
[7] M. Talmadge, C. Kinchin, H. Li Chum, A. de Rezende Pinho, M. Biddy, M.B.B. de Almeida, L. Carlos Casavechia, Techno-economic analysis for co-processing fast pyrolysis liquid with vacuum gasoil in FCC units for second-generation biofuel production, Fuel 293 (2021) 119960, https://doi.org/10.1016/j.fuel.2020.119960.
[8] G. Fogassy, N. Thegarid, Y. Schuurman, C. Mirodatos, From biomass to bio-gasoline by FCC co-processing: Effect of feed composition and catalyst structure on product quality, Energ. Environ. Sci. 4 (2011) 5068–5076, https://doi.org/10.1039/c1ee02012a.
[9] C. Liu, Y. Deng, Y. Pan, Y. Gu, B. Qiao, X. Gao, Effect of ZSM-5 on the aromatization performance in cracking catalyst, J. Mol. Catal. A Chem. 215 (2004) 195–199, https://doi.org/10.1016/j.molcata.2004.02.001.
[10] Z. Gholami, F. Gholami, Z. Tišler, M. Tomas, M. Vakili, A review on production of light olefins via fluid catalytic cracking, Energies 14 (2021) 1089, https://doi.org/10.3390/en14041089.
[11] A. Farshi, F. Shaiyegh, S.H. Burogerdi, A. Dehgan, FCC process role in propylene demands, Pet. Sci. Technol. 29 (2011) 875–885, https://doi.org/10.1080/10916460903451985.
[12] A. Akah, M. Al-Ghrami, Maximizing propylene production via FCC technology, Appl. Petrochem. Res. 5 (2015) 377–392, https://doi.org/10.1007/s13203-015-0104-3.
[13] G. Busca, Acid catalysts in industrial hydrocarbon chemistry, Chem. Rev. 107 (2007) 5366–5410, https://doi.org/10.1021/cr068042e.
[14] J. Čejka, B. Wichterlová, Acid-catalyzed synthesis of mono-and dialkyl benzenes over zeolites: Active sites, zeolite topology, and reaction mechanisms, Catal. Rev. Sci. Eng. 44 (2002) 375–421, https://doi.org/10.1081/CR-120005741.
[15] Precedence Research, Propylene Market.Global Industry Analysis, Size, Share, Growth, Trends, Regional Outlook, and Forecast 2023-2032, (2023). https://www.precedenceresearch.com/propylene-market (accessed March 4, 2024).
[16] A. Primo, H. Garcia, Zeolites as catalysts in oil refining, Chem. Soc. Rev. 43 (2014) 7548–7561, https://doi.org/10.1039/c3cs60394f.
[17] J. Přech, P. Pizarro, D.P. Serrano, J. Čejka, From 3D to 2D zeolite catalytic materials, Chem. Soc. Rev. 47 (2018) 8263–8306, https://doi.org/10.1039/c8cs00370j.
[18] A.A. Gusev, A.C. Psarras, K.S. Triantafyllidis, A.A. Lappas, P.A. Diddams, Effect of steam deactivation severity of ZSM-5 additives on LPG olefins production in the FCC process, Molecules 22 (2017) 1784, https://doi.org/10.3390/molecules22101784.
[19] Y. Ji, H. Yang, W. Yan, Strategies to enhance the catalytic performance of ZSM-5 zeolite in hydrocarbon cracking: A review, Catalysts 7 (2017) 367, https://doi.org/10.3390/catal7120367.
[20] S. Xia, Y. Zhu, Y. Tian, X. He, L. Guo, C. Qiao, G. Liu, Fe–Al isomorphous and self-pillared ZSM-5 nanosheet catalyst for cracking of n-heptane with enhanced selectivity of light olefins, J. Energy Inst. 102 (2022) 196–205, https://doi.org/10.1016/j.joei.2022.03.008.
[21] L. Wang, B. Peng, A. Zheng, Y. Song, Q. Jiang, P. Wang, H. Song, W. Lin, M. He, Mechanistic origin of transition metal modification on ZSM-5 zeolite for the ethylene yield enhancement from the primary products of n-octane cracking, J. Catal. 416 (2022) 387–397, https://doi.org/10.1016/j.jcat.2022.11.010.
[22] N. Rahimi, R. Karimzadeh, Catalytic cracking of hydrocarbons over modified ZSM-5 zeolites to produce light olefins: A review, Appl. Catal. A 398 (2011) 1–17, https://doi.org/10.1016/j.apcata.2011.03.009.
[23] E. Mohiuddin, M.M. Mdleleni, D. Key, Catalytic cracking of naphtha: The effect of Fe and Cr impregnated ZSM-5 on olefin selectivity, Appl. Petrochem. Res. 8 (2018) 119–129, https://doi.org/10.1007/s13203-018-0200-2.
[24] W.-C. Cheng, R. Kumar, M.S. Krishnamoorthy, M.S. Ziebarth, P.S. Deitz, Pentasil catalyst for light olefins in fluidized catalytic units, US Pat. 20090134065A1 (2009).
[25] M. Allahverdi, P. Diddams, C. Kanyi, Maximization of light olefins in FCC process, US Pat. US011524926B2 (2022).
[26] J. Zhang, X. Tang, H. Yi, Q. Yu, Y. Zhang, J. Wei, Y. Yuan, Synthesis, characterization and application of Fe-zeolite: A review, Appl. Catal. A 630 (2022) 118467, https://doi.org/10.1016/j.apcata.2021.118467.
[27] C. T-W Chu, C.D. Chang, Isomorphous substitution in zeolite frameworks. 1. Acidity of surface hydroxyls in [B]-, [Fe]-, [Ga]-, and [Al]-ZSM-5, J. Phys. Chem. 89 (1985) 1569–1571. https://doi.org/doi.org/10.1021/j100255a005.
[28] G. Berlier, G. Spoto, S. Bordiga, G. Ricchiardi, P. Fisicaro, A. Zecchina, I. Rossetti, E. Selli, L. Forni, E. Giamello, C. Lamberti, Evolution of extraframework iron species in Fe silicalite: 1. Effect of Fe content, activation temperature, and interaction with redox agents, J Catal 208 (2002) 64–82, https://doi.org/10.1006/jcat.2002.3535.
[29] A. Kurbanova, D. Zákutná, K. Gołąbek, M. Mazur, J. Přech, Preparation of Fe@MFI and CuFe@MFI composite hydrogenation catalysts by reductive demetallation of Fe-zeolites, Catal. Today 390–391 (2022) 306–315, https://doi.org/10.1016/j.cattod.2021.09.029.
[30] P. Ratnasamy, R. Kumar, Ferrisilicate analogs of zeolites, Catal. Today (1991) 329–416, https://doi.org/10.1016/0920-5861(91)80001-P.
[31] J. Rouquerol, F. Rouquerol, P. Llewellyn, G. Maurin, K. Sing, Adsorption by powders and porous solids: principles, methodology and applications, 2nd ed., Academic press, 2013.
[32] S. Lowell, J.E. Shields, M.A. Thomas, M. Thommes, Characterization of porous solids and powders: surface area, pore size and density, Springer Science & Business Media, 2004.
[33] B.C. Lippens, J.H. De Boer, Studies on Pore Systems in Catalysts V. The t Method, J. Catal. 4 (1965) 319–323, https://doi.org/10.1016/0021-9517(65)90307-6.
[34] Z. Klencsár, Mössbauer spectrum analysis by Evolution Algorithm, Nucl. Inst. Methods Phys. Res. B 129 (1997) 527–533, https://doi.org/10.1016/S0168-583X(97)00314-5.

[35] V. Zholobenko, C. Freitas, M. Jendrlin, P. Bazin, A. Travert, F. Thibault-Starzyk, Probing the acid sites of zeolites with pyridine: Quantitative AGIR measurements of the molar absorption coefficients, J. Catal. 385 (2020) 52–60, https://doi.org/10.1016/j.jcat.2020.03.003.
[36] L. Pinard, K. Ben Tayeb, S. Hamieh, H. Vezin, C. Canaff, S. Maury, O. Delpoux, Y. Pouilloux, On the involvement of radical "coke" in ethanol conversion to hydrocarbons over H-ZSM-5 zeolite, Catal Today 218–219 (2013) 57–64. https://doi.org/10.1016/j.cattod.2013.03.039.
[37] J.H. Yun, R.F. Lobo, Catalytic dehydrogenation of propane over iron-silicate zeolites, J. Catal. 312 (2014) 263–270, https://doi.org/10.1016/j.jcat.2014.02.007.
[38] G. Qi, R.T. Yang, Selective catalytic oxidation (SCO) of ammonia to nitrogen over Fe/ZSM-5 catalysts, Appl. Catal. A 287 (2005) 25–33, https://doi.org/10.1016/j.apcata.2005.03.006.
[39] P. Hudec, A. Smieskova, Z. Zidek, M. Zubek, P. Schneider, M. Kocirik, J. Kozankova, Adsorption properties of ZSM-5 zeolites, Collect. Czech. Chem. Commun. 63 (1998) 141–154, https://doi.org/10.1135/cccc19980141.
[40] S. Brunauer, L.S. Deming, W.S. Demming, E. Teller, On a Theory of the van der Waals Adsorption of Gases, Proc. Roy. Soc 69 (1937) 10, https://doi.org/10.1021/ja01864a025.
[41] M. Thommes, K. Kaneko, A.V. Neimark, J.P. Olivier, F. Rodriguez-Reinoso, J. Rouquerol, K.S.W. Sing, Physisorption of gases, with special reference to the evaluation of surface area and pore size distribution (IUPAC Technical Report), Pure Appl. Chem. 87 (2015) 1051–1069, https://doi.org/10.1515/pac-2014-1117.
[42] S. Bordiga, R. Buzzoni, F. Geobaldo, C. Lamberti, E. Giamello, A. Zecchina, G. Leofanti, G. Petrini, G. Tozzola, G. Vlaic, Structure and reactivity of framework and extra-framework iron in Fe-silicalite as investigated by spectroscopic and physicochemical methods, J. Catal. 158 (1996) 486–501, https://doi.org/10.1006/jcat.1996.0048.
[43] M.S. Kumar, M. Schwidder, W. Grünert, A. Brückner, On the nature of different iron sites and their catalytic role in Fe-ZSM-5 DeNOx catalysts: New insights by a combined EPR and UV/VIS spectroscopic approach, J. Catal. 227 (2004) 384–397, https://doi.org/10.1016/j.jcat.2004.08.003.
[44] E.J.M. Hensen, Q. Zhu, M.M.R.M. Hendrix, A.R. Overweg, P.J. Kooyman, M. V. Sychev, R.A. Van Santen, Effect of high-temperature treatment on Fe/ZSM-5 prepared by chemical vapor deposition of FeCl3: I. Physicochemical characterization, J. Catal. 221 (2004) 560–574, https://doi.org/10.1016/j.jcat.2003.09.024.
[45] M.S. Kumar, J. Pérez-Ramírez, M.N. Debbagh, B. Smarsly, U. Bentrup, A. Brückner, Evidence of the vital role of the pore network on various catalytic conversions of N2O over Fe-silicalite and Fe-SBA-15 with the same iron constitution, Appl. Catal. B 62 (2006) 244–254, https://doi.org/10.1016/j.apcatb.2005.07.012.
[46] K. Lázár, R. Fricke, H. Kosslick, J. Čejka, G. Vorbeck, A.M. Szeleczky, In situ studies of various forms of iron in MFI ferrisilicates*, in: Stud Surf Sci Catal, 1995: pp. 219–225. https://doi.org/10.1016/S0167-2991(06)81225-5.
[47] K. Lázár, G. Borbély, H. Beyer, In situ Mössbauer study of framework-substituted (Fe)ZSM-5 zeolites, Zeolites 11 (1991) 214–222, https://doi.org/10.1016/S0144-2449(05)80222-2.
[48] K. Góra-Marek, K. Brylewska, K.A. Tarach, M. Choi, Quantitative aspects of the identification of Fe(II) moieties in ZSM-5 zeolites with various pore hierarchies, Dalton Trans. 44 (2015) 8031–8040, https://doi.org/10.1039/c5dt00424a.
[49] E.P. Parry, An Infrared Study of Pyridine on Acidic Solids. Characterization of surface acidity., J Catal 2 (1963) 371–379. https://doi.org/10.1016/0021-9517(63)90102-7.
[50] K. Hadjiivanov, Identification and Characterization of Surface Hydroxyl Groups by Infrared Spectroscopy, in: Advances in Catalysis, Academic Press Inc., 2014: pp. 99–318. https://doi.org/10.1016/B978-0-12-800127-1.00002-3.
[51] A. Corma, A.V. Orchillés, Current views on the mechanism of catalytic cracking, Microporous and Mesoporous Mater. 35 (2000) 21–30, https://doi.org/10.1016/S1387-1811(99)00204-8.
[52] S. Kotrel, H. Knözinger, B.C. Gates, The Haag-Dessau mechanism of protolytic cracking of alkanes, Microporous Mesoporous Mater. 35 (2000) 11–20, https://doi.org/10.1016/S1387-1811(99)00204-8.
[53] F.-M. Pan, P.C. Stair, T.H. Fleisch, Chemisorption of pyridine and pyrrole on iron oxide surfaces studied by XPS, Surf. Sci. 177 (1986) 1–13, https://doi.org/10.1016/0039-6028(86)90253-0.
[54] G. Busca, V. Lorenzelli, Infrared study of chemisorption and reactivity of pyridine on haematite, Mater. Chem. 6 (1981) 175–186, https://doi.org/10.1016/0390-6035(81)90040-7.
[55] Y. Zhang, L. Qi, A. Lund, P. Lu, A.T. Bell, Mechanism and Kinetics of Acetone Conversion to Isobutene over Isolated Hf Sites Grafted to Silicalite-1 and SiO2, J. Am. Chem. Soc. 143 (2021) 8352–8366, https://doi.org/10.1021/jacs.1c01315.
[56] J. Pérez-Ramírez, J.C. Groen, A. Brückner, M.S. Kumar, U. Bentrup, M.N. Debbagh, L.A. Villaescusa, Evolution of isomorphously substituted iron zeolites during activation: Comparison of Fe-beta and Fe-ZSM-5, J. Catal. 232 (2005) 318–334, https://doi.org/10.1016/j.jcat.2005.03.018.
[57] R. Gounder, E. Iglesia, Catalytic consequences of spatial constraints and acid site location for monomolecular alkane activation on zeolites, J. Am. Chem. Soc. 131 (2009) 1958–1971, https://doi.org/10.1021/ja808292c.
[58] C. Chizallet, C. Bouchy, K. Larmier, G. Pirngruber, Molecular Views on Mechanisms of Brønsted Acid-Catalyzed Reactions in Zeolites, Chem. Rev. 123 (2023) 6107–6196, https://doi.org/10.1021/acs.chemrev.2c00896.
[59] V.B. Kazansky, M. V Frash, R.A. Van Santen, A quantum-chemical study of adsorbed nonclassical carbonium ions as active intermediates in catalytic transformations of paraffins. II. Protolytic dehydrogenation and hydrogen-deuterium hetero-isotope exchange of paraffins on high-silica zeolites, Catal Letters 28 (1994) 211–222. https://doi.org/10.1007/BF00806050.
[60] G.N. Vayssilov, H.A. Aleksandrov, E. Dib, I.M. Costa, N. Nesterenko, S. Mintova, Superacidity and spectral signatures of hydroxyl groups in zeolites, Microporous Mesoporous Mater. 343 (2022) 112144, https://doi.org/10.1016/j.micromeso.2022.112144.
[61] A. Chatterjee, T. Iwasaki, T. Ebina, A. Miyamoto, Density functional study for estimating Brønsted acid site strength in isomorphously substituted ZSM-5, Microporous Mesoporous Mater. 21 (1998) 421–428, https://doi.org/10.1016/S1387-1811(98)00051-1.
[62] J. Čejka, A. Vondrová, B. Wichterlová, G. Vorbeck, R. Fricke, The effect of AI, Fe, and In substitution in the MFI silicate structure on the aromatic hydrocarbon transformation: Si-OH-M site strength, Zeolites 14 (1994) 147–153, https://doi.org/10.1016/0144-2449(94)90009-4.
[63] Bart De Graaf, Mehdi Allahverdi, Martin Evans, Paul Diddams, "Snakes and ladders" for maximising propylene, PTQ (2014) Q4. www.digitalrefining.com/article/1001011.
[64] S. Creci, X. Wang, P.A. Carlsson, M. Skoglundh, Tuned Acidity for Catalytic Reactions: Synthesis and Characterization of Fe- and Al-MFI Zeotypes, Top. Catal. 62 (2019) 689–698, https://doi.org/10.1007/s11244-019-01155-4.
[65] H. Zhang, Y. Wang, S. Shao, R. Xiao, Catalytic conversion of lignin pyrolysis model compound-guaiacol and its kinetic model including coke formation, Sci. Rep. 6 (2016) 37513, https://doi.org/10.1038/srep37513.
[66] S. Altwasser, C. Welker, Y. Traa, J. Weitkamp, Catalytic cracking of n-octane on small-pore zeolites, Microporous Mesoporous Mater. 83 (2005) 345–356, https://doi.org/10.1016/j.micromeso.2005.04.028.
[67] M. Guisnet, N.S. Gnep, D. Aittaleb, Y.J. Doyemet, Conversion of light alkanes into aromatic hydrocarbons VI. Aromatization of C&C, Reaction mechanisms alkanes on H-ZSM-5, Appl Catal A Gen 87 (1992) 255–270. https://doi.org/10.1016/0926-860X(92)80060-P.
[68] T. Shoinkhorova, T. Cordero-Lanzac, A. Ramirez, S.H. Chung, A. Dokania, J. Ruiz-Martinez, J. Gascon, Highly selective and stable production of aromatics via high-pressure methanol conversion, ACS Catal. 11 (2021) 3602–3613, https://doi.org/10.1021/acscatal.0c05133.
[69] E.A. Uslamin, H. Saito, N. Kosinov, E. Pidko, Y. Sekine, E.J.M. Hensen, Aromatization of ethylene over zeolite-based catalysts, Catal, Sci. Technol. 10 (2020) 2774–2785, https://doi.org/10.1039/c9cy02108f.
[70] J.B. Taboada, A.R. Overweg, M.W.J. Crajé, I.W.C.E. Arends, G. Mul, A.M. Van Der Kraan, Systematic variation of 57Fe and Al content in isomorphously substituted 57Fe-ZSM-5 zeolites: preparation and characterization, Microporous Mesoporous Mater. 75 (2004) 237–246, https://doi.org/10.1016/j.micromeso.2004.07.024.